



A transient radial cortical microtubule array primes cell division in Arabidopsis

Isaty Melogno, Shogo Takatani, Paula Llanos, Coralie Goncalves, Chie Koderu, Marjolaine Martin, Claire Lionnet, Magalie Uyttewaal, Martine Pastuglia, Christophe Trehin, et al.

► To cite this version:

Isaty Melogno, Shogo Takatani, Paula Llanos, Coralie Goncalves, Chie Koderu, et al.. A transient radial cortical microtubule array primes cell division in Arabidopsis. Proceedings of the National Academy of Sciences of the United States of America, 2024, 121 (29), pp.e2320470121. 10.1073/pnas.2320470121 . hal-04691139

HAL Id: hal-04691139

<https://hal.science/hal-04691139v1>

Submitted on 7 Sep 2024

HAL is a multi-disciplinary open access archive for the deposit and dissemination of scientific research documents, whether they are published or not. The documents may come from teaching and research institutions in France or abroad, or from public or private research centers.

L'archive ouverte pluridisciplinaire **HAL**, est destinée au dépôt et à la diffusion de documents scientifiques de niveau recherche, publiés ou non, émanant des établissements d'enseignement et de recherche français ou étrangers, des laboratoires publics ou privés.

A transient radial cortical microtubule array primes cell division in Arabidopsis

Isaty Melogno¹⁺, Shogo Takatani^{1,2+}, Paula Llanos³, Coralie Goncalves⁴, Chie Koder⁴,
Marjolaine Martin¹, Claire Lionnet¹, Magalie Uyttewaal⁴, Martine Pastuglia⁴, Christophe
Trehin¹, David Bouchez⁴, Jacques Dumais³, Olivier Hamant^{1,*}

+ Equal contributions

¹ Laboratoire de Reproduction et Développement des Plantes, Université de Lyon, ENS de
Lyon, UCBL, INRAE, CNRS, 46 Allée d'Italie, 69364 Lyon Cedex 07, France

² Department of Biological Science, Graduate School of Science, Nagoya University, Furo-
cho, Chikusa-ku, Nagoya, 464-8602, Japan

³ Faculty of Engineering and Sciences, Universidad Adolfo Ibáñez, Av. Padre Hurtado 750,
Viña del Mar, Region of Valparaíso, Chile.

⁴ Université Paris-Saclay, INRAE, AgroParisTech, Institut Jean-Pierre Bourgin (IJPB), 78000,
Versailles, France

* Correspondence : Olivier Hamant : olivier.hamant@ens-lyon.fr

ABSTRACT

Because all cells experience mechanical stress, they have to develop resistance mechanisms to survive. In plants, this notably involves guidance of cellulose deposition by cortical microtubules in the direction of maximal tensile stress. Although the formation of new walls during cell division tends to follow maximal tensile stress direction too, analyses of individual cells over time reveal a much more variable behavior. The origin of such variability, as well as the exact role of interphasic microtubule behavior before cell division have remained mysterious so far. To approach this question, we took advantage of the Arabidopsis stem, where the tensile stress pattern is both highly anisotropic and stable. Although cortical microtubules generally align with maximal tensile stress, we detected a specific time window, ca. 3 hours before cell division, where cells form a radial pattern of cortical microtubules. This pattern was

observed in different growth conditions, and was not related to cell geometry or polar auxin transport. Interestingly, this cortical radial pattern correlated with the well-documented increase of cytoplasmic microtubule accumulation before cell division. This radial organization was prolonged in cells of the *trm678* mutant, where cortical microtubules are partially disorganized. Whereas division plane orientation in *trm678* is noisier, we found that cell division symmetry was in contrast more precise. We propose that an increased cytoplasmic microtubule accumulation in late G2 disrupts cortical microtubules alignment with tissue stress, allowing the cell to transiently explore its own geometry in order to select a future division plane with correct orientation and symmetry.

SIGNIFICANCE STATEMENT

In all kingdoms, cells divide according to their own geometry as well as external cues. We discovered a transient stage in plant cells, where part of the division machinery becomes blind to mechanical forces originating from the tissue. Using quantitative imaging and mutant analysis, we propose that this new pre-mitotic stage allows cells to take their own geometry into account and increase the precision of the following division.

INTRODUCTION

Cell division is first and foremost a geometric question: cells generally divide along a given division plane orientation, and more or less symmetrically, as defined by the relative volume of the two daughter cells. How mitosis operates is now well described in all kingdoms(1). However, we lack a clear understanding of how the cell division machinery achieves precision (i.e. reducing the variance in symmetric division) despite broad variation in cell shapes and division rates.

In *Drosophila* epithelia, cell division symmetry does not occur by default, but instead involves an active process. A “reset” stage indeed occurs, where cells become round. This pre-mitotic cell rounding has been proposed to allow cells to identify their centroid, thus triggering more symmetric divisions, independently of extracellular cues(2). Conversely, disruption of cell rounding in myosin motor mutants puts more weight on pre-mitotic cell geometry, through the maintenance of cell packing, thus biasing division plane orientation(3). Whether this also affects the precision of cell division symmetry remains unknown.

In plants, the presence of stiff cell walls mechanically hinders any cell deformation before mitosis. However, in late G2, the cortex of plant cells becomes largely depopulated of cortical microtubules (CMTs), and a dense ring forms, named the preprophase band (PPB). This transient pre-mitotic structure precisely predicts the position of the future division plane, established at cytokinesis. Since its discovery, the PPB was thought to be an essential attribute of cell division in most plants tissues(4), until specific PPB-less mutants were obtained and shown to have only mild developmental defects, at least under controlled conditions(5)(6). Furthermore, the PPB contributes to the robustness of division plane orientation, independently of division symmetry, since both symmetrically and asymmetrically dividing cells produce a PPB. Strongly asymmetric divisions, as in meristemoid cells, involve polarity cues that are inherited from interphase(7). However, this does not apply to most plant tissues, where cells divide symmetrically. How plant cells control the symmetry of division and its robustness is mostly unknown.

During interphase, the parallel alignment of CMTs has been shown to regulate the deposition of cellulose microfibrils in the wall(8). With few exceptions, the PPB, formed in G2 prior to mitosis, adopts the same orientation as the former interphasic cortical array(9). In addition, CMTs have also been found to align with maximal tensile stress in different organs or conditions(10). Because of the co-alignment between interphasic CMTs, PPB and division plane over time, division planes are also often aligned with maximal tensile stress(11). This provides a scenario in which plant cells and tissues would resist tensile stress, through cellulose-dependent wall reinforcement during interphase and new cell wall formation at mitosis, all parallel to maximal tensile stress orientation.

However, this scenario suffers from a number of experimental and conceptual issues. In particular, CMTs are not always co-aligned during interphase. For instance, basket/star configurations have been reported in hypocotyl cells(12). Besides, CMT array orientation is not necessarily homogeneous within a cell, and can change over time, for instance displaying global rotations(13), consistent with cellulose deposition dynamics too(14). Whether such behaviors could be reconciled with a response to tensile stress and the control of cell division remains to be investigated.

Here, using the *Arabidopsis* stem as a model system, and taking advantage of its stereotypical tissue stress pattern, we identified a transient radial CMT organization that appears prior to PPB formation, and that diverges from alignment with tissue stress. We propose that this reflects a stage where, in preparation to mitosis, cells sense their own geometry rather than tissue-related cues.

RESULTS

A stereotypical radial CMT organization before cell division

To observe CMTs in dividing cells over time, we used plant lines expressing the MAP4 microtubule binding domain (MBD) fused to mCitrine and focused our analysis on dissected shoot apices, as previously described(15), but here with higher spatial and temporal resolution (see Material and Methods).

In the Shoot Apical Meristem (SAM), as previously reported, we typically observed CMT alignment at the tissue scale, with a bias towards circumferential direction in the organogenetic (peripheral) zone, whereas and no particular bias was observed in the central zone (Figure 1A)(16). However, when considering individual cells over time, CMT behavior appeared much more variable. In particular, before cell division, we often observed cells with radial CMT orientations, as viewed from the top (Figure 1B, Figure S1A and S1B).

To explore this further, we needed higher spatial resolution. This led us to analyze this behavior in the stem from *in vitro*-grown plants. We focused on the stem region immediately below the shoot apical meristem, a region of active cell division, where cells are 2 to 3-fold larger (Figure 1C). Using cell-cell adhesion mutants, we previously demonstrated that the *Arabidopsis* stem exhibits a stereotypical and stable tensile stress pattern, with a maximum in the transverse orientation(17). In this tissue, we confirmed the presence of a strong and global bias of CMTs, towards the circumferential orientation (see Figure S2), parallel to the predicted maximal tensile stress (Figure 1C)(17). Again, when analyzing individual cells over time, we consistently observed a switch from the interphasic alignment of the MT array to a radial array before the formation of the PPB (Figure 1D). In order to increase the number of observable dividing cells,

we analyzed cell division in stems from plants grown *in-vitro* on cytokinin-supplemented medium (ACM medium). This readily increased the number of dividing cells imaged in time-lapses: we observed 24 dividing cells on 2 independent stems on ACM medium, vs. 13 dividing cells on 4 independent stems on the growth Arabidopsis Medium (AM)). A transient radial CMT behavior could be observed in all cases (Figure 1E). Note that this result was also confirmed when using a *pUBQ10::RFP-TUA6* marker line, albeit with lower spatial resolution (Figure S3A). From 5 time-lapse experiments with a time resolution of 1 hour, we estimated that this behavior preferentially occurred around 3 hours before cell division, lasts for about 1 hour, and is followed by the formation of the PPB (Figure 1D).

To go beyond these qualitative observations, we measured the distribution of orientations of the CMT arrays using the Directionality plugin in ImageJ for each time-lapse experiment. In all quantifications, time 0 corresponds to the closest timepoint preceding nuclear envelope breakdown, as inferred from the disruption of the PPB, and the initiation of the mitotic spindle. As expected, at $t = -4$ hours, we found a bias towards the transverse orientation (-2.8° at -4 hours; 1st quartile = -10.6° , 3rd quartile = 12.1°), which corresponds to the transverse axis of the stem (also the predicted maximal tensile stress direction) (Figure 1G, $n=34$ cells). From 1 hour before $t=0$ up to PPB formation, CMT arrays also exhibited an orientation bias, reflecting the PPB orientation (Figure 1G, $n=37$ cells). However, 3 to 2 hours before $t=0$, the bias was much weaker (-11.9° at -3 hours; 1st quartile = -65.7° , 3rd quartile = 20.2° ; -23.6° at -2 hours; 1st quartile = -90° , 3rd quartile = 5.1°) (Figure 1G, $n=35$ cells). To assess the statistical differences between CMT orientation distribution at each timepoints, we performed Kolmogorov-Smirnoff tests. We found differences to be statistically significant between -2 or -3 hours and earlier timepoints, meaning that the radial array of CMTs appear significantly different from previous interphasic CMT co-alignments (Figure S4). As a negative control, we also found no statistical differences between the distributions at -6 hours and -5 hours, or between the distributions at -3 hours and -2 hours, at a threshold of 0.05 (Figure S4).

To confirm this observation, we used the FibrilTool plugin in ImageJ(18) to quantify the anisotropy of the CMT arrays in each cell and analyzed the anisotropy distribution per time point (Figure S3B). This analysis revealed a drop in the anisotropy value two to three hours before $t=0$ (Figure 1H, $n=36$ cells). Anisotropy then increased again from 1 hour before $t=0$ up to PPB maturation (Figure 1H, $n=38$ cells). Based on these quantifications, we established that, in the stem, the radial array starts ca. 3 hours before the PPB formation and lasts for ca. 2 hours

167 until the start of the PPB maturation. This finding thus challenges the often assumed continuity
168 between interphasic CMTs and PPB ([Figure 1F](#)). We propose to call this stage where CMTs
169 form a radial pattern 3 hours before cell division, the “radial step”.

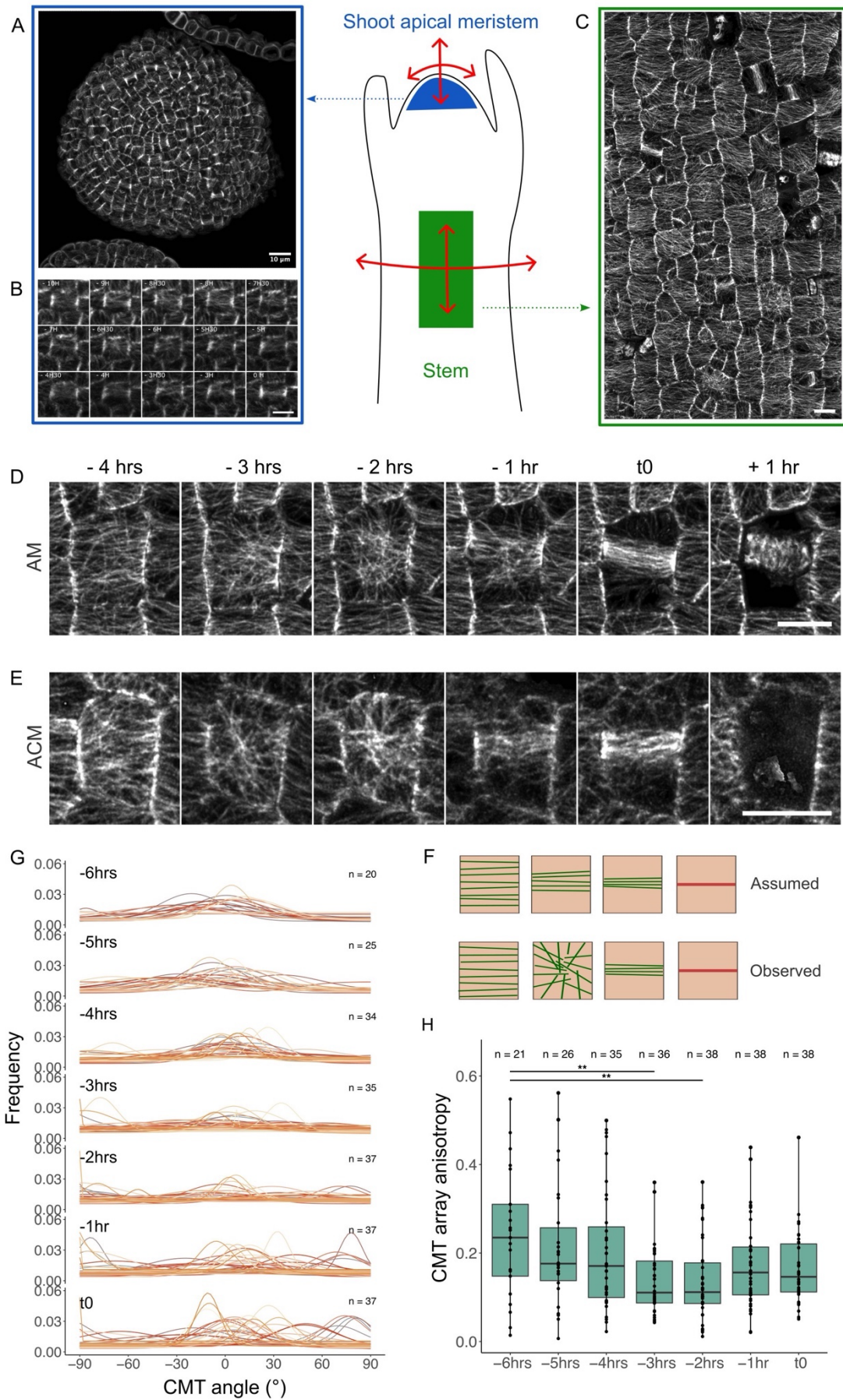


Figure 1. A transient pre-PPB radial pattern of CMTs in the meristem and the stem.

(A) Top view of the shoot apical meristem expressing the *pPDF1::mCitrine-MBD* marker. Red arrows indicate a predicted isotropic tensile stress pattern in the central zone. (B) Time-lapse of a pre-mitotic cell of the SAM, showing the CMT dynamics before the formation of the PPB, using the *pPDF1::mCitrine-MBD* marker line. CMT organization changes from co-aligned arrays (-10h to -7h30) to radial arrays (-7h to -6h) before the start of PPB maturation. (C) Side view of the stem expressing the *pPDF1::mCitrine-MBD* marker. Red arrows indicate the transverse direction of maximal tensile stress, as demonstrated in(17). (D, E) Time lapse of pre-mitotic cells in the stem, showing CMT dynamics before PPB formation, using the *pPDF1::mCitrine-MBD* marker line on the growth medium (AM, D) and cytokinin-supplemented medium (ACM, E). Note the presence of radial CMTs ca. 3 hours before cell division. (F) Schematic summary of the transition between the aligned, interphasic CMT array and the PPB array. The top panel illustrates the simplest scenario, and the bottom panel recapitulates the observations made with the time-lapse experiments. (G) Distribution of CMT orientations overtime in cells from the stem. The angle scale varies between -90° and +90°, 0° being the transverse orientation to the stem axis. Each row represents the time before t=0 (last timepoint before the nuclear envelope breakdown). Each color-coded curve represents the results obtained for one cell. (H) Graphical representation of the evolution of the anisotropy values obtained with FibrilTool overtime (** *p*-value < 0.01, Tuckey test). For all images in this figure, SurfCut projections were used, projecting the mCitrine signal between 0 and 4 μm from the surface. The Brightness & Contrast parameters have been modified for a better visualization of CMTs. Scale bars: 10 μm (A, C); 5 μm (B, D, E).

The radial step can be uncoupled from cell shape and final division plane orientation

To assess whether the radial step relates to cell division plane orientation, we analyzed its behavior in cells of different shapes. In stem tissues, isodiametric cells tend to divide perpendicular to the stem axis (Figure 2B), whereas elongated cells tend to divide along the shortest plane (Figure 2C). Such difference could be related to cellular stress patterns, as inferred from the curvature of the outer wall: the shape of elongated cells prescribes transverse derived maximal tensile stress direction whereas the shape of isodiametric cells prescribes isotropic tensile stress direction(11) (Figure 2A). Note that in contrast to the tensile stress

pattern in the stem, which was experimentally validated(17), this cell-shape-derived stress pattern is only predicted from a pressure vessel model of an epidermal cell(11)(19). We thus explored whether the radial step may depend on differences in cell shape and/or related stress pattern.

To monitor this quantitatively, we calculated the cell aspect-ratio and plotted cell division orientation with respect to the stem axis, using either the PPB as a predictor of the future division plane, or the plasma membrane resulting from a division (Figure 2D, n=141 cells). This confirmed a dual behavior according to cell aspect ratio, at least for cells with an extreme aspect ratio. In particular, more isodiametric cells tend to display division planes perpendicular to the stem axis (i.e. parallel to predicted maximal tissue stress); whereas more elongated cells displayed division planes rather parallel to the stem axis (i.e. perpendicular to maximal tissue stress) (Figure 2D). In order to find the threshold value at which cells switch their behavior, we fitted a logistic regression using the binomial method of the generalized linear models in R (with a p -value of $3.40e^{-11}$). This method only partially fit the data ($R^2 = 0.312$), due to the noise in division orientation in either group, but allowed us to successfully retrieve an inflection point at 0.6 (Figure 2E, see Material and methods). To monitor the orientation of division relative to the cell axis, we measured the orientation of the long axis of the cell relative to the axis of the stem. Measuring the orientation of the long axis of the cell relative to the axis of the stem revealed that most anisotropically shaped cells were elongated transversely to the stem (“C cell” in Figure 2A, see Cell angle color code in Figure 2D), implying that their shortest axis, and thus the maximal tension derived from the cell shape, was orthogonal to the tissue-derived maximal tensile stress. Taking advantage of this dual behavior according to cell shape, we could confirm that in the stem, cells with an aspect ratio below 0.6 tend to divide following cell-shape-derived tension, respecting the local minima rule(20) (Besson and Dumais, 2011). The ones with an aspect ratio above 0.6 (rounder cells) would tend to divide following the tissue-derived maximal tensile stress, that is perpendicular to the stem axis.

Even though the conflict between maximal tension orientations derived from the cell shape or the tissue may affect the positioning of the division plane, the radial step was comparable in both types of cells, whether elongated (Figure 2B) or not (Figure 2C). We also confirmed this quantitatively with the Directionality measurements, by creating two data subsets: one for cells with a PPB oriented along the stem axis, and the other for cells with a PPB perpendicular to the stem axis. In both cases, the CMT array underwent the radial step (Figures S5A and S5B). To

further confirm that the radial step appears independently from final cell division plane orientation, we observed asymmetrically dividing cells in stems, and we could find a radial step again around 3 hours before cell division (Figure S3C and S3D).

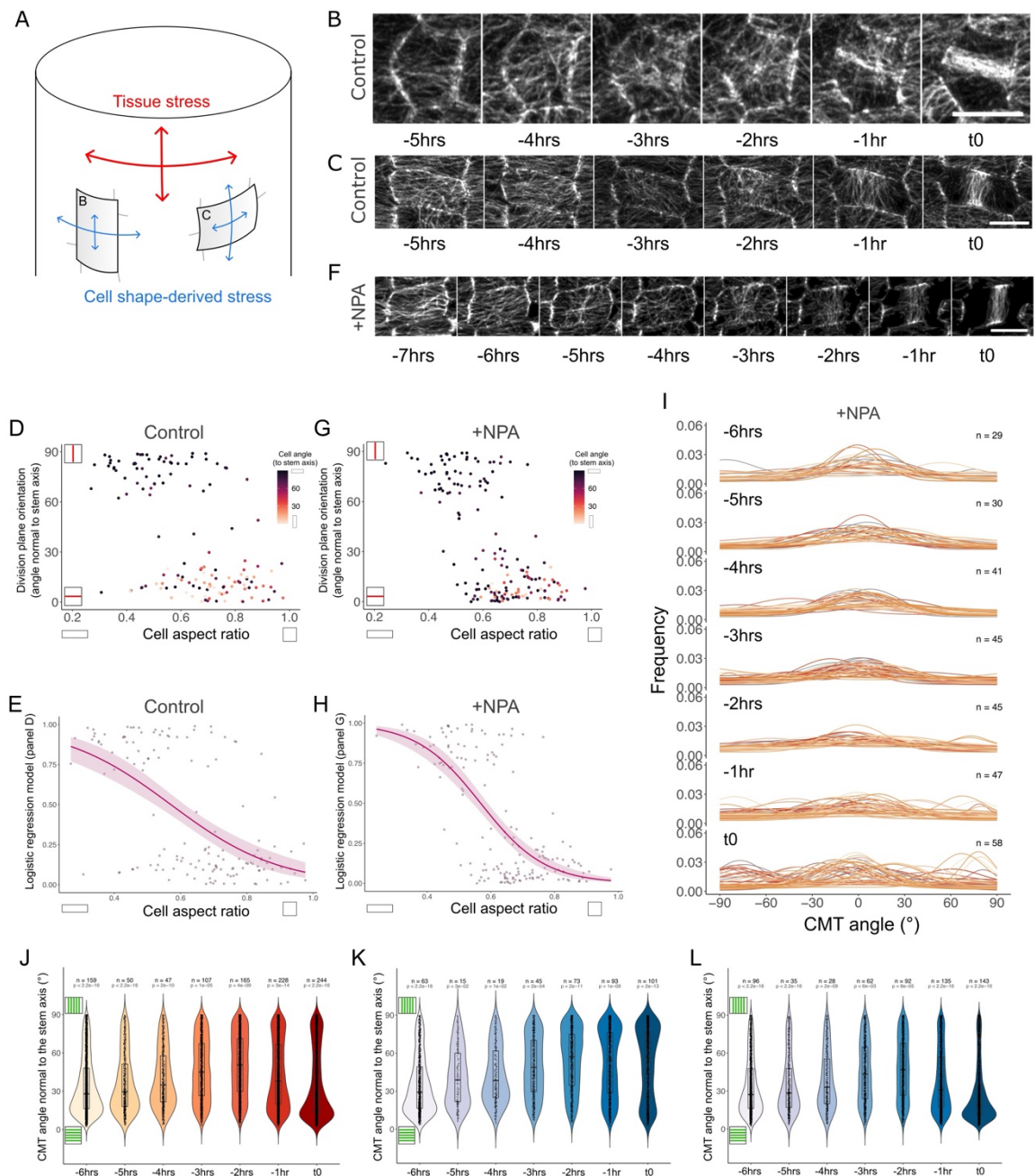


Figure 2. The radial step occurs independent of cell shape or polar auxin transport

(A) Diagram representing the predicted tensile stress patterns for epidermal cells in stems. The cylindrical shape of the stem prescribes maximal tensile stress transverse to the stem axis. At cell scale, the minor axis of the cell is also the predicted tensile stress maximal direction. Depending on cell orientation, tissue stress and cell shape-derived stress are synergistic or antagonistic (B) Representative example of a cell expressing the *pPDF1::mCitrine-MBD* marker, with its major axis parallel to the stem axis. The cell forms a radial CMT organization before dividing perpendicular to the stem axis. (C) Representative example of a cell expressing the *pPDF1::mCitrine-MBD* marker, with its major axis perpendicular to the stem axis. The cell forms a radial CMT organization before dividing parallel to the stem axis. (D) Dotplot representing the orientation relative to the stem of the PPB or division planes of cells, in the stem in function of their aspect ratio (the ratio between the longest and the shortest axis of an ellipse fitted around the cell contours). The color code reflects the angle between the major axis of the cell and the stem axis. Light colors highlight cells with their longest axis along the stem axis, dark colors highlight cells with their longest axis transverse to the stem axis. (E) Same as (D), with normalized the data to fit a logistic regression (scale 0 to 1), using the glm function in R studio ($R^2 = 0.312$). (F) Time lapse showing pre-miotic cells in the stem expressing the *pPDF1::mCitrine-MBD* marker, with NPA from germination. (G) Same as (D), with NPA from germination. (H) Same as (E), with NPA from germination ($R^2 = 0.457$). (I) Same as Figure 1D, with NPA from germination. (J) Distribution of CMT angles normal to the stem axis overtime from NPA-treated plants using the OrientationJ - vector field function in Fiji. The *p*-values correspond to the result of a Kolmogorov-Smirnoff statistical test comparing the distribution of the data to a uniform distribution. (K) same as (J) but for cells with an aspect ratio below 0.6 (most elongated cells). (L) same as (J) but for cells with an aspect ratio above 0.6 (most isodiametric cells). All images are SurfCut projections between 0 to 4 μm from the surface of the mCitrine signal. Scale bars: 5 μm .

The radial step can be uncoupled from polar auxin transport

Our analysis so far shows that the radial step is independent of cell shape variability. Next, we investigated whether the radial step depends on larger polarizing cues. To do so, we impaired polar auxin transport using Naphtylphtalamic acid (NPA), as auxin has previously been shown to affect cell division rate in roots(21) and plane orientation in embryos(22). We grew plants

on NPA-containing medium and, using the same *pPDF1::mCitrine-MBD* marker line, we observed the effect of NPA on CMT organization in stems. It is worth noting that the inhibition of flower formation on stems vastly facilitated the imaging and thus significantly increased sample size.

We observed the presence of the radial step before PPB formation in the presence of NPA as well (Figure 2F, n=58 cells). Note that the radial step could also be observed in the *pRPS5a::RFP-TUA5* marker line treated with NPA (Figure S3E). This demonstrates that the occurrence of the radial step is not dependent upon polar auxin transport. However, the duration of the radial step was longer with NPA (ca. 3 hours) than in its absence (ca. 2 hours) (Figure 2F and 2I, Figure S3E). While cells were usually more isodiametric on NPA than in absence of NPA, the division plane orientation followed a bimodal distribution (transverse or longitudinal) similar to untreated cells (Figure 2G and 2H, n=194 cells). We also fitted a logistic regression with the glm function in R to the data and found an inflection point at 0.6 as well (p -value < $2.2e^{-16}$). The function fit the data better than in control conditions ($R^2 = 0.457$), probably due to the larger sample size. This suggests that the observation that cells tend to divide following the maximal tension derived either from their shape, or from the tissue is dependent on their aspect ratio, remains true in NPA conditions. When dividing the data in two subsets (one for cells with PPBs following the stem axis, and one for cells with PPBs normal to the stem axis), we could also conclude that occurrence of the radial step is not dependent on the final position of the PPB (Figure S5C and S5D).

Taking advantage of the larger sample size, we next analyzed CMT orientation with respect to the stem axis in NPA-treated plants, using the OrientationJ plugin in Fiji. CMTs were highly perpendicular to the stem axis (i.e. parallel to predicted maximal tensile stress direction) before -3 hours (Figure 2J), and this trend was transiently lost between -4 hours and -3 hours, with a more uniform distribution of CMT orientations reflecting the radial step (Figure 2J). We then did the same analysis for cells with an aspect-ratio below 0.6 (i.e. the most elongated cells, Figure 2K) and above 0.6 (i.e. the most isodiametric cells, Figure 2L). The conclusions were conserved, further confirming that the radial step is independent of cell shape and auxin transport. In the end, most of the elongated cells divided parallel to the stem axis (i.e. perpendicular to maximal tensile stress direction, Figure 2K), in contrast to most isodiametric cells, which divided perpendicular to the stem axis (i.e. parallel to maximal tensile stress

direction, [Figure 2L](#)). This analysis further confirms that the presence radial step is not dependent on the final cell division plane orientation.

The radial step coincides with the pre-mitotic increase in cytoplasmic microtubule content and is prolonged when this process is promoted

Because the radial step occurs independently of microtubule markers used, growth media or polar auxin transport, we hypothesized that its presence and timing of appearance is mainly controlled by intrinsic factor(s). In plants, and contrary to many eucaryotes, there is no microtubule organizing center (MTOC) and the formation of new microtubules is mostly distributed, and strongly relies on microtubule-dependent γ -tubulin recruitment and branched nucleation(23)(24)(25). Consistently, γ -tubulin mutants display mitotic and interphasic microtubule defects(26). However, there are multiple evidence of microtubule nucleation specifically at the nuclear envelope(27)(28) at the end of the G2 phase, before and during PPB formation(29)(9)(23). This well-established behavior is generally thought to ensure a connection between the PPB and the nucleus(9)(23), and to provide a population of peri-nuclear microtubules to complete mitotic tasks, such as spindle formation(30)(31). Here we investigated whether this behavior also occurs in the stem and whether it temporally correlates with the radial step.

To assess the cytoplasmic microtubule content, we analyzed the microtubule signal in XZ maximal projections, i.e. through anticlinal cell sections, and calculated the ratio between the endoplasmic signal and the cortical signal. As expected, we observed a gradual increase of the internal microtubule content as the cell reached the PPB stage, with an average increase between the first and the last timepoints of 162% ([Figure 3A and 3B](#), see [Figure S7A](#)). Cytoplasmic microtubules started to accumulate around 3 hours before cell division, i.e. coincident with the radial step.

To test the connection between the radial step and cytoplasmic microtubule accumulation, we next investigated the radial step in a *trm678* mutant background, grown and imaged in control conditions, as described for the WT. This mutant, as other PPB-deficient mutants, displays a strong accumulation of perinuclear MTs before mitosis(5)(6). The *fass* mutant exhibits an increased microtubule nucleation(32), and this could be a feature of most TTP complex

mutants, such as *trm678*, with some evidence pointing towards this hypothesis⁴. Because *ton1* and *fass* mutants exhibit very disrupted interphasic microtubules(5), this would hinder the analysis of more subtle changes in CMT behavior, and notably the radial step. Among these PPB-deficient mutants, *trm678* exhibit WT-like interphasic microtubules(6) (Figure S6A), allowing us to investigate the radial step behavior in that background.

The mitotic index was comparable in WT and *trm678* stems (1.56% +/- 1.04% in WT stems, and 2.00% +/- 1.21% in *trm678* stems). In the stem, the average duration of mitosis was roughly 50% longer in *trm678* (ca. 3 hours) than in the WT (ca. 2 hours, Figure S6B and S6C), even though the exact difference is difficult to assess due to our time resolution. As previously seen in the wild-type, we observed a radial step in *trm678* stems (Figure 3C, n= 29 cells). As expected for a PPB-deficient mutant, the division orientations in the *trm678* stems were noisier than in of the WT (Figure 3C)(33), further confirming that the radial step appears independent of final cell division plane orientation. However, the radial step exhibited two unique features in *trm678*. First, it seemed visually clearer than in the WT (Figure 3C). To ascertain this, we measured the anisotropy of CMT arrays, and found it to be twice lower 3 hours before cell division in the *trm678* mutant compared to the WT, consistent with the observation of a better-defined radial step (p -value = $6,05e^{-6}$ at -2 hours, TuckeyHSD test; Figure 3F). Second, the radial step appeared to last much longer than in the WT. The exact average duration of the radial step in *trm678* is difficult to estimate, because in most of our kinetics, the radial step lasted at least 6 hours, and we missed the full sequence (from interphasic CMTs to the radial step to mitosis) within a multi-hour kinetics (Figure 3C and Figure S6A). We could observe that switch only in exceptional cases, i.e. when the radial step was shorter (ca. 4 hours) before cell division (Figure S7B). In the *trm678* mutant, the internal microtubule signal was significantly higher than in the WT, as shown when following individual kinetics (Figure 3D, Figure S7) and when pooling measurements (a 213% increase between $t = -6$ hours and $t = 0$, p -value = $2.38e^{-4}$ for *trm678*, and a 162 % increase between $t = -6$ hours and $t = 0$, p -value = 0.062 for the WT, Wilcoxon test, Figure 3E). We also measured the anisotropy of CMT array, using ImageJ FibrilTool, and observed reduced anisotropy in *trm678* on average, when compared to WT, consistent with the prolonged radial step in the mutant (Figure 3F). This analysis further suggests that the transient radial organization of CMTs reflects the start of cytoplasmic microtubule accumulation before cell division.

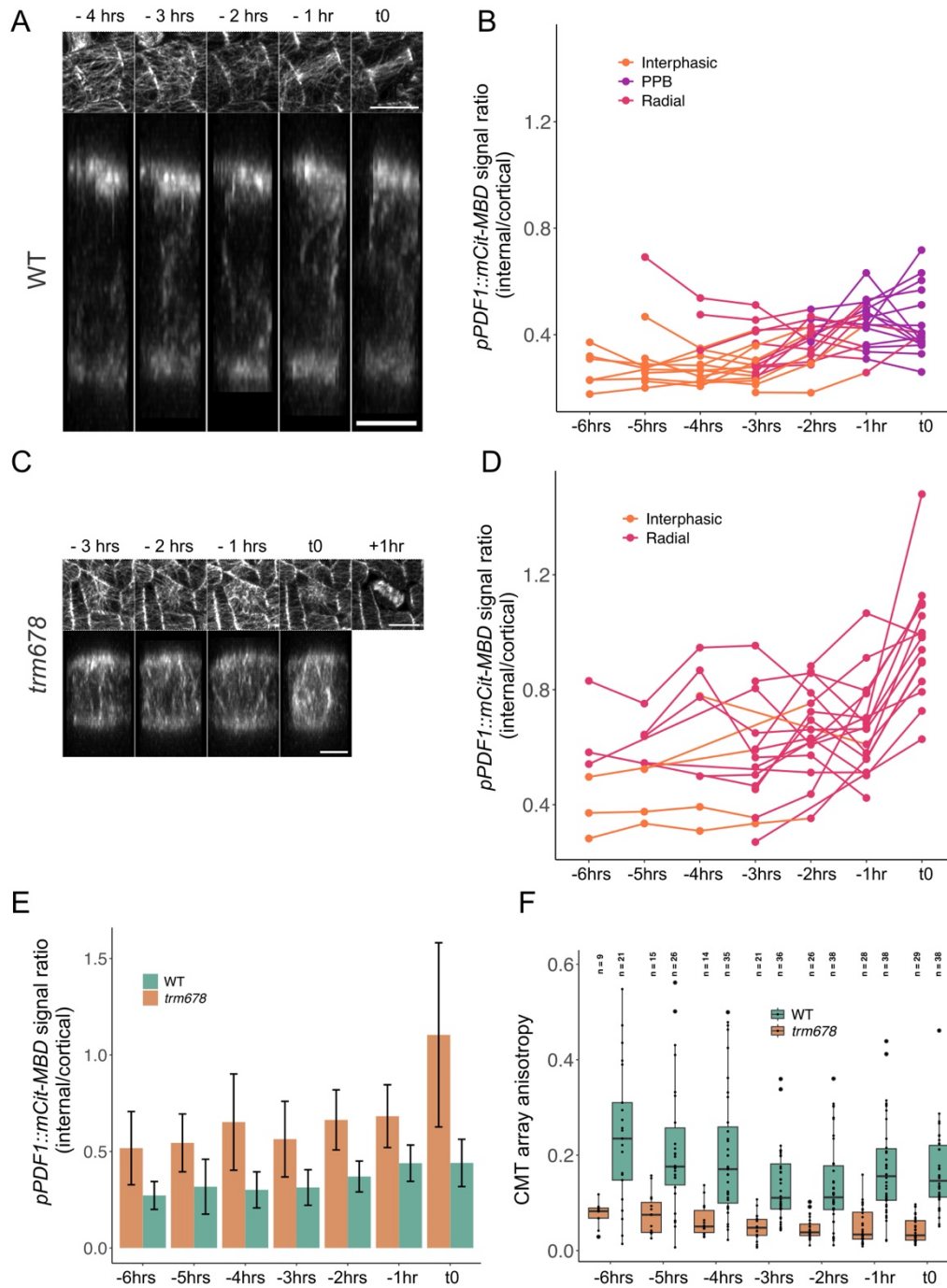


Figure 3. The radial array of CMTs correlates with a pre-mitotic increase of internal microtubule content.

(A-D) Evolution of cytoplasmic microtubules overtime in WT background (A) or in the *trm678* mutant background (C). (A) Time-lapse images of pre-mitotic cells, the top panel being the cortical projection with SurfCut and the bottom panel an orthogonal projection through the cell.

Cortex images are 8-bit, with the B&C range varying between 0 and 160, and orthogonal projections are 16-bit, with the B&C range varying between 0 and 1400. (B) Ratio between the average internal signal and the average of the cortical mCitrine-MBD signal over time. The colors correspond to qualitative classifications of cortical arrays (interphasic, radial step and PPB). Each line represents the kinetics for a given cell. (C) same as (A) but in the *trm678* mutant. (D) same as (B) but in the *trm678* mutant. (E) Evolution of the ratio of mCitrine-MBD signal (internal/cortical) overtime in WT vs. *trm678*. (F) Evolution of CMT array anisotropy overtime, using the FibrilTool plugin in Fiji. Results from the WT are reproduced here from Figure 1H for ease of reading, to compare with *trm678*. Scale bars: 10 μ m (surface projections), 5 μ m (orthogonal projections).

Disruption in the balance between cortical and cytoplasmic microtubule accumulation in *trm678* increases the precision of cell division

Altogether, the radial organization of CMTs coincides with increased cytoplasmic microtubule accumulation around the nucleus (Figure S8), which is even more pronounced in the absence of TRM6/7/8. This provides a scenario in which the radial step emerges from a destabilization of CMTs, either from increased connections between CMTs and the nucleus, or from competition between different sites of microtubule nucleation. This also transiently disrupts CMT alignment with tensile stress at the outer periclinal wall. What could be the function of this reset sequence?

The reset stage where cells become blind to their mechanical environment echoes data in *Drosophila* epithelia where cell rounding occurs to allow the cell to perceive its centroid, independently from adjacent cells influence, in order to define the degree of cell division symmetry(2)(3). The radial step may have a comparable function in plants, in terms of shielding. Indeed, the inner periclinal cortex also displays a radial reorganization of the CMT array before the formation of the PPB (Figure S9).

To address this question, we analyzed daughter cell volumes in WT and *trm678* stems, and plotted the volumes ratio for both genotypes. The mean ratios were comparable (1.30 +/- 0.26 in WT vs. 1.20 +/- 0.14 in *trm678* (Figure 4A)). Note that the means are higher than 1 because we measure the ratio between the larger daughter cell over the smaller one. Interestingly, while

the averages were not significantly different (Wilcoxon test p -value = 0.253), the variances were significantly different (0.07 in WT and 0.02 in *trm678*, Fligner test p -value = 0.005), *trm678*'s symmetry between daughter cells being 3.79 times less variable than in wild-type. This suggests that a longer and better-defined radial step correlates with more precise divisions, reducing the variability in daughter cell volume ratios.

Because the *trm678* has a prolonged radial step and a prolonged M phase (Figure S6B), we next checked whether increased precision is simply the result of a slower pre-mitotic stage. To do so, we performed the same analysis in NPA-treated WT plants, which exhibit slightly longer radial step and slightly longer mitosis than non-NPA treated plants. This did not affect the variance of daughter cell volumes (Figure 4A). When performing the same analysis on NPA-treated *trm678* stems, we instead observed a partial rescue: the variance in NPA-treated *trm678* stems was lower than NPA-treated WT stems, but higher than control *trm678* stems (Figure 4A). Thus, the precision in cell division does not correlate with a slower pre-mitosis and mitosis dynamics, but instead, with a longer and qualitatively more clear-cut radial step, in *trm678*. Altogether, we propose that the accumulation of cytoplasmic microtubules near the nuclear envelope 3 hours before cell division in stems transiently disrupts the co-alignment of CMTs with tensile stress, forming a radial organization of CMTs, thus allowing the cell to control the precision of its division, by becoming less sensitive to external cues.

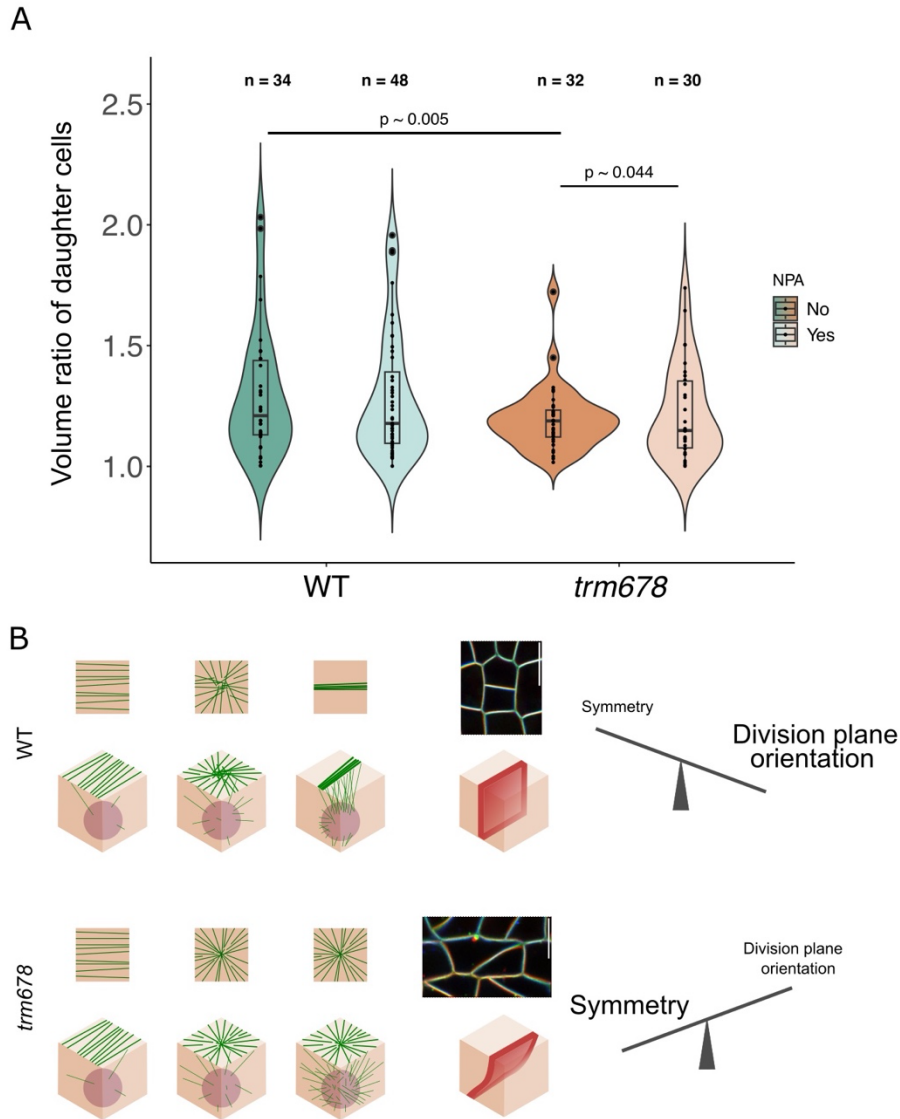


Figure 4. The radial step could be a marker for cell shape sensing and symmetry precision in assessing the division plane positioning.

(A) Violin plot showing the distribution of the ratio between the volume of the two daughter cells in WT and *trm678* backgrounds, in both control and NPA conditions. The measurements were made using images from cells expressing *pUBQ10::Lti6b-TdTomato* membrane marker. The ratio is always between the bigger daughter cell and the smaller daughter cell, for comparison purposes. The *p*-values displayed are the ones obtained from the Fligner's statistical test using R studio. (B) Model: In the WT (top panel), a suboptimal radial step allows the cell to sense its own geometry to define cell division symmetry loosely, while the formation of the PPB defines robust division plane orientation; in the *trm678* mutant (bottom panel), a better-

defined radial step improves the division precision (daughter cell volumes), to the detriment of division plane orientation robustness. Radial step and PPB reflect a trade-off in robustness (division precision vs. division plane orientation, respectively). Images: RGB projection of recently divided cells at different focal planes (red: top of the cell, green: middle of the cell, blue: bottom of the cell) in the WT (top cell) and *trm678* (bottom cell). Scale bars: 10 μ m.

DISCUSSION

Altogether, our results are consistent with a sequential model in which the progressive accumulation of cytoplasmic microtubules during the G2 phase would disrupt CMT alignment with tensile stress to allow the cell to sense its own geometry for a short time window and to ensure the precision of cell division. We do not exclude that this stage could also help the cell to acquire information on other key cell division parameters, such as centroid position(34). After this transitory stage, CMTs would resume their alignment either with the short axis of the cell when cells are elongated (Errera's rule, also matching cell-shape derived maximum of tensile stress) or with tissue stress, when cells are isodiametric, to control the final division plane orientation.

The transient CMT organization before mitosis as an exception to the CMT alignment with tensile stress

So far, the alignment of CMTs with maximal tensile stress has been verified in most plant tissues(35)(10), and suffers only a few exceptions. Although this needs to be formally investigated, most of these exceptions could be explained by invoking differences in stress levels. For instance, one could propose that a drop of turgor pressure in hypocotyls switching from dark to light could explain the rapid growth arrest and associated switch in CMT orientation(36). Similarly, the progressive reinforcement of cell walls during differentiation, and thus reduction in stress level, could explain the loss of CMT co-alignment in leaf epidermis(37). This notably builds on recent investigations in protoplasts that are confined in microwells: in this case, CMTs are transverse, aligned with the shortest axis of an elongated cells, which is also a local maximum of stress, following Laplace-Young law(38). However, when they are placed in a hyperosmotic medium, i.e. when tension decreases, CMTs switch to

the long axis of the cell: they follow the flattest part of the protoplast contour, which is also the minimum of bending energy(38)(39).

To our knowledge, the only undisputable exception of CMTs alignment with tensile stress is thus provided in this work, in the sense that during the timeframe of the radial step, the global pattern of tension should not change: 3 hours before cell division, cells in stems exhibit a radial organization of their CMT arrays. This cannot be explained by a change in tissue stress pattern, as adjacent cells usually exhibit CMTs that are aligned with predicted tissue stress direction. A change in cell wall properties would be too slow to affect the CMTs so transiently. Although we cannot exclude the possibility that turgor level would transiently change 3 hours before cell division, this would be unlikely to cause a radial CMT organization. As shown in the protoplast experiments, following a drop of turgor pressure, CMTs would align with the long axis of the cell, and would not make a radial pattern.

The radial CMT step as a reset mechanism

Our observation goes against a common assumption that PPB orientation usually follows that of CMT during interphase. We instead identified a reset stage where CMTs become disorganized for a duration of ca. 2 hour and at a well-defined time window (3 hours before cell division). The radial step reflects a stage during which CMTs switch from their role in guiding the deposition of cellulose microfibrils, to their role in controlling cell division. Other cortical microtubule arrays have been shown to have links with cell division (typically, the PPB, and more recently cortical-telophase microtubules(40)), further suggesting that close to mitosis, there is a change in CMTs function. Based on the temporal correlation between cytoplasmic microtubule enrichment during the G2 phase and on the prolongation and better-definition of the radial step when cytoplasmic microtubule accumulation is promoted (in *trm678*), we propose that the radial step is a period during which increased cytoplasmic microtubule accumulation disrupts the CMT self-organization, thereby making the CMT network transiently blind to external mechanical cues.

Our time-lapse analyses shed a new light on past reports on guard mother cells (GMCs). In particular, to quote Yoshinobu Mineyuki in 1999(41), notably building on studies by Mullinax and Palevitz in 1989(42), "graminean GMCs have "interphase microtubule bands" that orient perpendicular to PPBs. This transverse interphase microtubule band precedes a radial

microtubule array, which is then replaced by a PPB prior to the longitudinal cell division". These past reports together with our analysis suggest that the radial step is not a guard mother cell exception, but more likely the rule.

To go one step further, the proposed function of the radial step may be similar to the proposed role of the cell rounding step in *Drosophila* epithelia. Indeed, upon disruption of cell rounding through myosin motor inactivation, epithelial cells remain packed as they divide, and their division plane follows cell geometry instead of tissue stress(3). Even though the mechanical properties of a plant tissue are different than that of an animal due to the presence of cell walls, our analysis of cell division plane orientation according to cell aspect ratio also fits the idea that a threshold of stress, either prescribed by cell shape or tissue shape, determines the final orientation of division plane. Interestingly, in our study, we could explore the consequence of a prolonged, well-defined, radial step, and we found an increase in cell division volume precision. This opens the question as to whether this would also be true in *Drosophila* epithelia.

A trade-off in precision between division plane orientation and division precision

The idea of a competition between internal and cortical microtubules is not totally new. Indeed, cytoplasmic microtubules have major impacts on cortical array in non-dividing cells(43). Cytoplasmic microtubules can generate an isotropic array overriding the pre-existing microtubule array through the tethering function of CLASP(44). Because pre-mitotic cytoplasmic microtubules are prominent in late G2 phase, it could cause great impact on cortical microtubule array. This is what we find here, also revealing that the accumulation of cytoplasmic microtubules before cell division does not only serve as a reservoir of microtubules to prepare mitosis, but it also contributes to the precision of cell division, possibly by making the cell more self-centered on its nucleus.

We showed that the radial step is robust to different cell shapes, cell identity (shoot apical meristem, stem, meristemoids) and growth conditions (AM and ACM medium, with or without NPA), where cortical and cytoplasmic microtubule behavior is likely to vary. Such robustness may emerge from a more fundamental parameter: the conflict between cytoplasmic and cortical microtubules. Whereas long-term tracking of dividing cells with microtubule markers and at high enough resolution are still rare in the literature, we could find examples of *Datura stramonium* cells with a transient pattern reminiscent of what we observed in *Arabidopsis* (45).

We thus propose that the radial step reflects the sequential control of cell division, where division precision precedes division plane robustness. We can speculate that the radial step is an integral part of the preparation for mitosis and therefore could be extended to other tissues and cell types. This sequence also suggests that division precision is more variable than division plane orientation (as its control is temporally more distant from mitosis), possibly because a small error in division precision has less implications than a small error in division plane orientation, at least from a mechanical point of view.

MATERIAL AND METHODS

Plant material and growth conditions

All *Arabidopsis thaliana* lines were in the Col-0 ecotype. Wild-type Col-0 and the *trm678* triple mutant(6) were transformed using the dipping floral method(46). Transgenic lines were expressing a microtubule marker (*pPDF1::mCitrine-MBD*(47)) and a plasma membrane marker (*pUBQ10::Lti6-TdTomato*(48)). As controls, we also used plants expressing the *pRPS5a::RFP-TUA5* tubulin marker, and plants expressing the *pUBQ10::RFP-TUA6* tubulin marker.

For SAM imaging, *Arabidopsis* Wild-type and *trm678* mutant lines were sown on soil and grown in climatic chambers under short-day conditions (8-h light/16-h dark) for 6 weeks and then grown under long-day conditions (16-h light /8-hdark regime) for 4 weeks. Dissected apices were embedded in ACM culture medium (2.2 g/L Murashige and Skoog medium without vitamins (Duscheffa), 10 g/L sucrose, pH 5.8 KOH (10 M), 8 g/L agarose) supplemented with 1x Morel and Wetmore vitamins and 570 nmol/L trans-zeatin (12.5ul of 1mg/mL of stock solution in 100ml of ACM medium), and maintained under long-day conditions (16-h light 8-h/dark regime, 21°C) as described in (49).

For stem imaging, seeds were sterilized using a sterilization solution (88 mg/mL sodium dichloroisocyanurate and 90% ethanol). 50 to 300 µL of seeds were first incubated in 1 mL of the sterilization solution for 6 minutes, and then washed twice with 96% ethanol and left to dry. Seeds were sown on solid *Arabidopsis* medium (11.82 g/L *Arabidopsis* medium (Duscheffa, a custom-made medium for the lab, recipe in the Supplementary Material), 2 mM Ca(NO₃)₂ 4H₂O, pH 5.8 KOH (10 M), 10 g/L granulated agar (Merck)). In NPA conditions, this medium

was supplemented with 10 μm of naphthylphthalamic acid (NPA). The seeds were left for stratification for 2 days at 4°C in the dark, and plants were grown for around 3 weeks in long day conditions (16h light/8h dark) at 20°C, until the first flower buds developed.

It is worth noting that, while the cell division is very active at the tip of the stem, imaging conditions can inhibit division and affect microtubule dynamics. This happened in both Arabidopsis and ACM media. We noticed that the winter season is usually more prone to induce slow division rates.

SAM dissection and imaging

Dissected shoot apices were imaged with a Leica SP8 upright confocal microscope (Figures 1A, 1B, and S1A). Confocal z-stacks were acquired (every 30 min for 10 hours) at a resolution of $0.09 \times 0.09 \times 0.2 \mu\text{m}$ per voxel using a HC FLUOTAR L 25x/0.95 N.A. water immersion objective. The confocal scan speed was no more than 7, and line averaging was set to 2.

Stem preparation and imaging

Arabidopsis stems from *in vitro* plants with a few unopened flower buds were selected. For easier dissection, we selected stems that were ca.1.5 cm long. Then, the organs impairing a correct imaging were dissected (cauline leaves and flower buds). The imaging medium was either the same as the growth medium (Arabidopsis Medium, AM), or Apex Culture Medium (ACM). In the NPA conditions, the ACM medium was supplemented with 10 μm of naphthylphthalamic acid (NPA). The plants with prepared stems were transferred to an imaging medium and fixed in the medium by placing the roots and leaves inside the agar, exposing the area of interest. The plate containing the samples was placed in the growing chamber for one day before the experiment. Figure S10A illustrates the different steps of stem preparation.

The images for all figures, except Figures 1A, 1B, S1A and S3A, were acquired using the LSM980 – Airyscan 2 upright confocal microscope (Zeiss). All the samples were imaged under the W Plan-Apochromat x20 water immersion lens (NA: 1.0), and were kept under immersion during the whole experiment. All images were made using the airyscan mode of the microscope. For this, the size of the image needed to be optimized for the Airyscan module, which resulted in a pixel size of around $0.065 \mu\text{m} \times 0.065 \mu\text{m}$. The Z resolution was always $0.500 \mu\text{m}$. The

pixel time could vary between experiments, but the scanning was always bidirectional and averaged twice by frame. Airyscan parameters are detailed in [Figure S10B](#).

Some of the images used for [Figures 2D-2G, 2H, 2I](#) acquired using the LSM980 – Airyscan 2 inverted confocal microscope (Zeiss). All the samples were imaged under the C-Apochromat x40 water immersion lens (NA: 1.2), and were kept under immersion during the whole experiment by placing a droplet of water directly on the objective. The rest of the parameters are the same as described above.

The images for [Figure S3A](#), as well as for the production of the measurements of [Figures 2D-E, 2G-H, 2J-2L](#) were acquired using the SP8 confocal microscope (Leica). The samples were imaged using a x25 water-immersion lens (NA = 0.95), with the resonant scanner switched off, to obtain better resolution. 8-bit images were taken in 1024x512 μm /pixels format, with the XY-resolution of 0.152 μm /pix and Z-stack slices of 0.500 μm . Images were acquired with a scanning speed of 1000 and averaged 4 times. The mCitrine signal was imaged using the 514 nm laser (0.5% intensity) and a HyD 1 detector between 518 nm and 549 nm. The results for [Figures 2D, 2G, 2E, 2H](#) were made using images from the three microscopes.

Image processing

All the processing of the images was done on the Fiji (ImageJ) software.

The LSM980 images were processed using the Airyscan Processing program in the Zeiss software, with the “All Images (2D)” program and the Auto Filter. They were then converted from the Carl Zeiss Image format (.czi) to Tagged Image Format File (.tiff) format, using a slightly modified version of the lifRxiv program (<https://github.com/sverger/lifRxiv>).

The SP8 images were converted from Leica Image File Format (.liff) to Tagged Image Format File (.tiff) format, using the lifRxiv program.

The image stacks were then processed using the SurfCut program⁽⁵⁰⁾ projecting the upper signal from the top slices (between 0 and 4 μm of the epidermis). The SurfCut projections coming from the same sample at different time points were then assembled into stacks. We selected the cells that divided or exhibited a PPB by the end of the time frame of the experiment.

635 **Division plane orientation analysis**

636 Cells of interest, showing either a PPB or a cell plate, were identified. The longest and shortest
637 axis were measured by manually drawing a region of interest to the cell's contours, and
638 extracting the fitted ellipse using Fiji. The aspect ratio was then obtained by dividing the
639 shortest plane by the longest plane of this fitted ellipse.

640 The orientation of the division plane, or the PPB, was also measured manually using the Fiji
641 software. The orientations were normalized to keep the results between 0° and 90°, with the
642 0° orientation being horizontal.

643 The division angles were all divided by 90, to get a dataset between 0 and 1, in order to perform
644 the logistic regression. The regression was made with the “glm” fit in R, with the “quasi-
645 binomial” family to account for the dispersion of the data, and the “logit” link. To assess the
646 goodness of the fit, we calculated the R-squared value using the null deviance, and the residual
647 deviance given by the glm function, as followed:

$$648 \quad R^2 = 1 - \left(\frac{\text{Residual deviance}}{\text{Null deviance}} \right)$$

649 To find an approximation of the inflection point of the fitted curve, we acknowledged that the
650 “logit” link uses the following regression:

$$651 \quad \log\left(\frac{p}{1-p}\right) = ax + b$$

652

653 With p being the probability of the response being 1, a being the slope, and b the intercept.

654 We therefore calculated x with p set at 0.5, and a and b being the result of the “glm” fit.

655 **Cortical microtubule orientation analysis**

656 We manually drew rectangles in the center of the cortex, avoiding the edges (to prevent biases
657 in the measurements) on SurfCut projections, for the cells of interest. To measure the local
658 orientations of microtubules overtime, we used the Directionality function in Fiji, using the

“Local gradient orientation” method. The output of this program is a distribution of the pixel orientations between -90° and 90° (with 0° being the vertical orientation), as well as a gaussian fit to the data. We plotted the gaussian fit, for each cell at each timepoint.

We used the OrientationJ package’s “vector field” function in Fiji (<http://bigwww.epfl.ch/demo/orientation/>) as another way of measuring CMT orientation (Figure 2J, 2K, 2L). For this, we wrote a homemade macro allowing to extract the vectors inside the region of interest. Briefly, we defined the ROI manually and blacken it. We then extract the coordinates of the vectors inside this blackened area by setting a threshold on the energy value given by the “vector field” output. Once these coordinates are saved, we run the “vector field” on the unchanged image and retain the orientation of the vectors of interest. To test the differences in the distribution of these vectors’ orientations overtime, we ran the Klotz-Smirnov test in RStudio. With this test, we compared the distribution of the data at each timepoint with a uniform sequence, generated with RStudio.

To measure the anisotropy of the microtubule arrays, we used the SurfCut images, and delimited the region of interest by hand, following the cell contour, but excluding the antinuclear cortex to avoid any bias. We ran the FibrilTool plugin(18) in Fiji to extract the anisotropy. To test the differences between the different genetic background and the different timepoints, we ran the Tukey-Kramer test in RStudio.

Cytoplasmic microtubule content analysis

To analyze the cytoplasmic microtubule, we used Z-stacks of images from lines expressing *pPDF1::mCitrine-MBD*. To project the cytoplasmic microtubule signal, we used the reslice function in Fiji, with “Output spacing” set at $0.5\ \mu\text{m}$, starting at the top. We then made a maximal projection of the reslice output to obtain the cytoplasmic microtubule signal. The region of interest for the reslice projection was determined by hand, by being careful of excluding the antinuclear cortex of the cell to only project the internal signal.

The outer perinuclear cortex, as well as the inside of the cell were marked by hand, and the average signal was measured using Fiji. For each cell, at each timepoint, the ratio between the internal signal and the cortical signal was plotted, to be able to compare all the measurements, and balance the photobleaching that the samples experienced overtime. We tested the

differences in these values between the different genetic backgrounds and between each timepoint using the Tukey-Kramer test in RStudio.

Volume measurements

Membrane marker images were resized to obtain a voxel size with a X of around 250 μm . The images were then processed using the MorphoGraphX software(51). First, images were blurred using the Gaussian blur stack function, and then the segmentation was made using the ITK Watershed Auto Seeded function, and the parameters were fine-tuned to obtain a suitable 3D segmentation. A mesh was then applied using the Marching Cube 3D function, and the volumes were extracted with the Cell Analysis 3D function.

Recent divisions were spotted by eye, as newer membranes separating two daughter cells are straight, anchored at 90° from the edges and are thinner than older membranes. The ratio between the two volumes was then always measured by dividing the bigger daughter cell's volume by the smaller ones. For statistical tests, we first performed a Wilcoxon test in RStudio, comparing the averages of the ratios with respect to the NPA conditions (with or without NPA), for each genetic background (WT and *trm678*). As there was not a statistically significant difference between the averages, with a threshold of 0.05, and due to the aspect of the data, we performed a Fligner's test in RStudio that focuses on the variances. The *p*-values are displayed on [Figure 4A](#).

ACKNOWLEDGMENTS AND FUNDING SOURCES

We thank the MechanoDevo team at the RDP lab for insightful discussion, and Platim for help with imaging. This work was supported by a Human Frontier Science Program Long-Term-Fellowship (LT000891/2018-L to S.T.), by the European Research Council (ERC-2021-AdG-101019515 "Musix" to O.H.) and by Human Frontier Science Program grant RGP0023/2018. This work has benefited from the support of IJPB's Plant Observatory technological platforms. The IJPB benefits from the support of Saclay Plant Sciences-SPS (ANR-17-EUR-0007).

REFERENCES

1. B. Alberts, *Molecular biology of the cell*, Seventh edition (W. W. Norton & Company, 2022).
2. M. P. Stewart, *et al.*, Hydrostatic pressure and the actomyosin cortex drive mitotic cell rounding. *Nature* **469**, 226–230 (2011).
3. S. Chanet, R. Sharan, Z. Khan, A. C. Martin, Myosin 2-Induced Mitotic Rounding Enables Columnar Epithelial Cells to Interpret Cortical Spindle Positioning Cues. *Curr. Biol.* **27**, 3350–3358.e3 (2017).
4. T. Sawidis, H. Quader, M. Bopp, E. Schnepf, Presence and absence of the preprophase band of microtubules in moss protonemata: a clue to understanding its function? *Protoplasma* **163**, 156–161 (1991).
5. J. Traas, *et al.*, Normal differentiation patterns in plants lacking microtubular preprophase bands. *Nature* **375**, 676–677 (1995).
6. E. Schaefer, *et al.*, The preprophase band of microtubules controls the robustness of division orientation in plants. *Science* **356**, 186–189 (2017).
7. A. Muroyama, D. Bergmann, Plant Cell Polarity: Creating Diversity from Inside the Box. *Annu. Rev. Cell Dev. Biol.* **35**, 309–336 (2019).
8. A. R. Paredez, C. R. Somerville, D. W. Ehrhardt, Visualization of cellulose synthase demonstrates functional association with microtubules. *Science* **312**, 1491–1495 (2006).
9. S. M. Wick, J. Duniec, Immunofluorescence microscopy of tubulin and microtubule arrays in plant cells. II. Transition between the pre-prophase band and the mitotic spindle. *Protoplasma* **122**, 45–55 (1984).
10. D.-C. Trinh, *et al.*, How Mechanical Forces Shape Plant Organs. *Curr. Biol.* **31**, R143–R159 (2021).
11. M. Louveaux, J.-D. Julien, V. Mirabet, A. Boudaoud, O. Hamant, Cell division plane orientation based on tensile stress in *Arabidopsis thaliana*. *Proc. Natl. Acad. Sci. U. S. A.* **113**, E4294–4303 (2016).
12. L. Vineyard, A. Elliott, S. Dhingra, J. R. Lucas, S. L. Shaw, Progressive transverse microtubule array organization in hormone-induced *Arabidopsis* hypocotyl cells. *Plant Cell* **25**, 662–676 (2013).
13. J. Chan, G. Calder, S. Fox, C. Lloyd, Cortical microtubule arrays undergo rotary movements in *Arabidopsis* hypocotyl epidermal cells. *Nat. Cell Biol.* **9**, 171–175 (2007).
14. J. Chan, *et al.*, The rotation of cellulose synthase trajectories is microtubule dependent and influences the texture of epidermal cell walls in *Arabidopsis* hypocotyls. *J. Cell Sci.* **123**, 3490–3495 (2010).
15. A. Burian, *et al.*, A correlative microscopy approach relates microtubule behaviour, local organ geometry, and cell growth at the *Arabidopsis* shoot apical meristem. *J. Exp. Bot.* **64**, 5753–5767 (2013).
16. O. Hamant, *et al.*, Developmental patterning by mechanical signals in *Arabidopsis*. *Science* **322**, 1650–1655 (2008).
17. S. Verger, Y. Long, A. Boudaoud, O. Hamant, A tension-adhesion feedback loop in plant epidermis. *eLife* **7** (2018).
18. A. Boudaoud, *et al.*, FibrilTool, an ImageJ plug-in to quantify fibrillar structures in raw microscopy images. *Nat. Protoc.* **9**, 457–463 (2014).
19. A. Sampathkumar, *et al.*, Subcellular and supracellular mechanical stress prescribes cytoskeleton behavior in *Arabidopsis* cotyledon pavement cells. *eLife* **3** (2014).
20. S. Besson, J. Dumais, Universal rule for the symmetric division of plant cells. *Proc. Natl. Acad. Sci. U. S. A.* **108**, 6294–6299 (2011).
21. H. Ai, *et al.*, Auxin-dependent regulation of cell division rates governs root thermomorphogenesis. *EMBO J.* **42**, e111926 (2023).

22. S. Yoshida, *et al.*, Genetic control of plant development by overriding a geometric division rule. *Dev. Cell* **29**, 75–87 (2014).
23. B. Liu, J. Marc, H. C. Joshi, B. A. Palevitz, A γ -tubulin-related protein associated with the microtubule arrays of higher plants in a cell cycle-dependent manner. *J. Cell Sci.* **104**, 1217–1228 (1993).
24. H. C. Joshi, B. A. Palevitz, γ -Tubulin and microtubule organization in plants. *Trends Cell Biol.* **6**, 41–44 (1996).
25. T. Murata, *et al.*, Microtubule-dependent microtubule nucleation based on recruitment of γ -tubulin in higher plants. *Nat. Cell Biol.* **7**, 961–968 (2005).
26. M. Pastuglia, *et al.*, γ -Tubulin Is Essential for Microtubule Organization and Development in *Arabidopsis*. *Plant Cell* **18**, 1412–1425 (2006).
27. K. Mizuno, Microtubule-nucleation sites on nuclei of higher plant cells. *Protoplasma* **173**, 77–85 (1993).
28. V. Stoppin, Isolated Plant Nuclei Nucleate Microtubule Assembly: The Nuclear Surface in Higher Plants Has Centrosome-like Activity. *PLANT CELL ONLINE* **6**, 1099–1106 (1994).
29. J. Chumová, H. Kourová, L. Trögelová, P. Halada, P. Binarová, Microtubular and Nuclear Functions of γ -Tubulin: Are They LINCed? *Cells* **8**, 259 (2019).
30. M. Yamada, G. Goshima, Mitotic Spindle Assembly in Land Plants: Molecules and Mechanisms. *Biology* **6**, 6 (2017).
31. Y. J. Lee, B. Liu, Microtubule nucleation for the assembly of acentrosomal microtubule arrays in plant cells. *New Phytol.* **222**, 1705–1718 (2019).
32. A. Kirik, D. W. Ehrhardt, V. Kirik, TONNEAU2/FASS regulates the geometry of microtubule nucleation and cortical array organization in interphase *Arabidopsis* cells. *Plant Cell* **24**, 1158–1170 (2012).
33. C. B. Scott, *et al.*, Graph metric learning quantifies morphological differences between two genotypes of shoot apical meristem cells in *Arabidopsis*. *Silico Plants* **5**, diad001 (2023).
34. J. Moukhtar, *et al.*, Cell geometry determines symmetric and asymmetric division plane selection in *Arabidopsis* early embryos. *PLOS Comput. Biol.* **15**, e1006771 (2019).
35. O. Hamant, D. Inoue, D. Bouchez, J. Dumais, E. Mjolsness, Are microtubules tension sensors? *Nat. Commun.* **10**, 2360 (2019).
36. J. J. Lindeboom, *et al.*, A mechanism for reorientation of cortical microtubule arrays driven by microtubule severing. *Science* **342**, 1245533 (2013).
37. F. Zhao, *et al.*, Microtubule-Mediated Wall Anisotropy Contributes to Leaf Blade Flattening. *Curr. Biol. CB* **30**, 3972-3985.e6 (2020).
38. L. Colin, *et al.*, Cortical tension overrides geometrical cues to orient microtubules in confined protoplasts. *Proc. Natl. Acad. Sci. U. S. A.* **117**, 32731–32738 (2020).
39. P. Durand-Smet, T. A. Spelman, E. M. Meyerowitz, H. Jönsson, Cytoskeletal organization in isolated plant cells under geometry control. *Proc. Natl. Acad. Sci.* **117**, 17399–17408 (2020).
40. M. A. Bellinger, *et al.*, Cortical microtubules contribute to division plane positioning during telophase in maize. *Plant Cell* **35**, 1496–1512 (2023).
41. Y. Mineyuki, “The Preprophase Band of Microtubules: Its Function as a Cytokinetic Apparatus in Higher Plants” in *International Review of Cytology*, (Elsevier, 1999), pp. 1–49.
42. J. B. Mullinax, B. A. Palevitz, Microtubule reorganization accompanying preprophase band formation in guard mother cells of *Avena sativa* L. *Protoplasma* **149**, 89–94 (1989).
43. C. Ambrose, G. O. Wasteneys, Microtubule Initiation from the Nuclear Surface Controls Cortical Microtubule Growth Polarity and Orientation in *Arabidopsis thaliana*. *Plant Cell Physiol.* **55**, 1636–1645 (2014).
44. P. Y. Le, C. Ambrose, CLASP promotes stable tethering of endoplasmic microtubules

to the cell cortex to maintain cytoplasmic stability in *Arabidopsis* meristematic cells. *PLOS ONE* **13**, e0198521 (2018).

45. D. J. Flanders, D. J. Rawlins, P. J. Shaw, C. W. Lloyd, Nucleus-associated microtubules help determine the division plane of plant epidermal cells: avoidance of four-way junctions and the role of cell geometry. *J. Cell Biol.* **110**, 1111–1122 (1990).

46. S. J. Clough, A. F. Bent, Floral dip: a simplified method for *Agrobacterium*-mediated transformation of *Arabidopsis thaliana*: Floral dip transformation of *Arabidopsis*. *Plant J.* **16**, 735–743 (1998).

47. A. Armezzani, *et al.*, Transcriptional induction of cell wall remodelling genes is coupled to microtubule-driven growth isotropy at the shoot apex in *Arabidopsis*. *Dev. Camb. Engl.* **145** (2018).

48. C. W. Melnyk, C. Schuster, O. Leyser, E. M. Meyerowitz, A Developmental Framework for Graft Formation and Vascular Reconnection in *Arabidopsis thaliana*. *Curr. Biol.* **25**, 1306–1318 (2015).

49. O. Hamant, P. Das, A. Burian, “Time-Lapse Imaging of Developing Shoot Meristems Using A Confocal Laser Scanning Microscope” in *Plant Cell Morphogenesis, Methods in Molecular Biology.*, F. Cvrčková, V. Žárský, Eds. (Springer New York, 2019), pp. 257–268.

50. Ö. Erguvan, M. Louveaux, O. Hamant, S. Verger, ImageJ SurfCut: a user-friendly pipeline for high-throughput extraction of cell contours from 3D image stacks. *BMC Biol.* **17**, 38 (2019).

51. P. Barbier de Reuille, *et al.*, MorphoGraphX: A platform for quantifying morphogenesis in 4D. *eLife* **4**, 05864 (2015).

Supplementary Information for:

A transient radial cortical microtubule array is involved in premitotic control of cell division in Arabidopsis

Isaty Melogno¹⁺, Shogo Takatani^{1,2+}, Paula Llanos³, Chie Kodera⁴, Marjolaine Martin¹, Claire Lionnet¹, Magalie Uyttewaal⁴, Martine Pastuglia⁴, Christophe Trehin¹, David Bouchez⁴, Jacques Dumais³, Olivier Hamant^{1,*}

Table 1. Detail of the composition of the Arabidopsis medium.

Arabidopsis medium	
Formula	mg/mL
CoCl ₂ .6H ₂ O	0.0025
CuSO ₄ .5H ₂ O	0.13
Ferric Ammonium Citrate	50
NaCl	0.58
H ₃ BO ₃	4.33
MnCl ₂ .4H ₂ O	2.77
Na ₂ MoO ₄ .2H ₂ O	0.05
ZnSO ₄ .7H ₂ O	0.29
KH ₂ PO ₄	340.25
KNO ₃	500.5
MgSO ₄ .7H ₂ O	246.5
Myo-Inositol	100
Nicotinic Acid	1
Pyridoxine HCl	1
Thiamine HCl	1
Ca-Panthotenate	1
Biotine	0.01
Sucrose	10000
MES	700

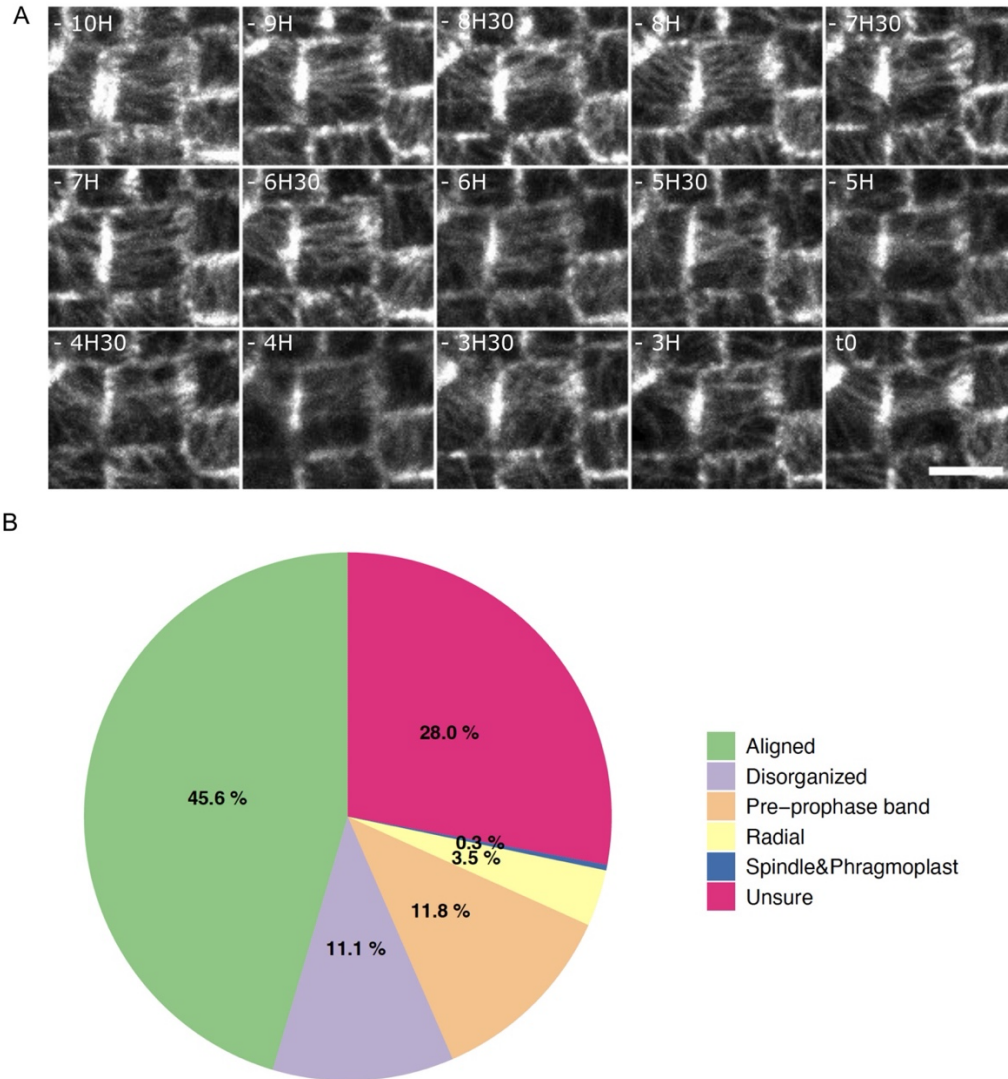


Figure S1. Radial array of CMTs in pre-mitotic cells at the shoot apical meristem

(A) Other example of a time lapse showing cortical microtubules dynamics before the establishment of the PPB. From -10 hours to -6 hours, CMTs maintain a stable orientation. From -5h30 onwards, CMTs exhibit less consistent orientations, up to PPB formation. Images are SurfCut projections of the area between 0 and 4 μm of the surface of the *pPDF1::mCit-MBD* signal. The scale bar corresponds to 5 μm . The Brightness and Contrast parameters have been modified for a better visualization of the microtubules. (B) Pie chart representing the average percentages of the different organizations of CMT arrays in shoot apical meristems. Aligned reflect the directional organization, typically at interphase. PPB corresponds to the cells where a clear band of microtubules is observed. Radial shows the radial array we described above. Spindle/Phragmoplast corresponds to cells that are undergoing mitosis. Disorganized is when the array is visible, but all of the above categories are not suited to describe it, whereas unsure reflects cells where no clear classification could be made (either the resolution was too low or the image was blurry). These classifications were made qualitatively on a total of 4 shoot apical meristems, where only the central zone was observed.

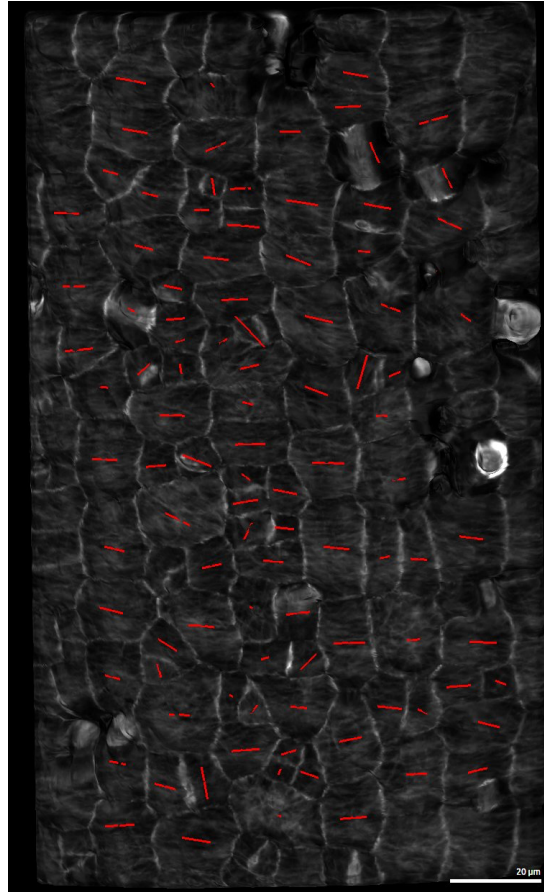


Figure S2. Average CMT orientations in an *Arabidopsis* stem.

This image represents the projection of the *pPDF1::mCitrine-MBD* signal between 0 and 4 μm , using the MorphoGraphX software. Cells were segmented using this software, and the average orientation of CMTs was extracted and displayed. The red lines represent the average orientation of CMTs. The length of the line corresponds to the anisotropy of the CMT arrays: the longer the line, the higher the anisotropy value. Most of the cells display transverse cortical microtubules, following the predicted maximal tensile stress pattern.

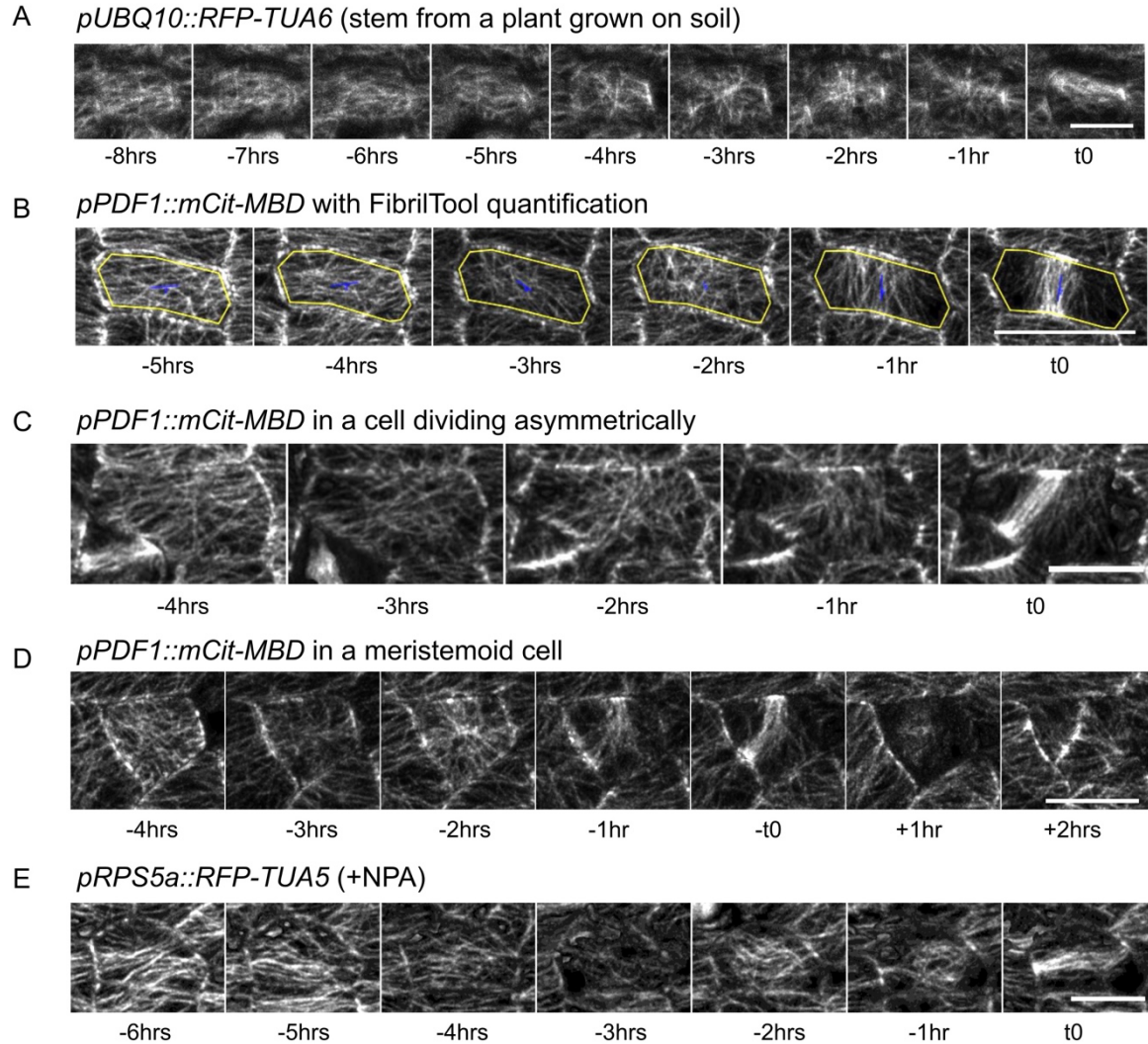


Figure S3. Additional evidence of radial CMTs before cell division

(A) CMT dynamics before cell division in stems, using the *pUBQ10::RFP-TUA6* marker line grown on soil. (B) Example of FibrilTool measurement: the yellow contour defines the region of interest from which the measurements are made. The blue line represents the anisotropy of the CMT arrays with its length, and the predominant orientation of the CMTs with its orientation. (C) Example of CMT dynamics in an asymmetrically dividing cell. (D) Example of CMT dynamics in a meristemoid cell (dividing asymmetrically). (E) CMT dynamics before cell division in stems, using the *pRPS5a::RFP-TUA5*, with NPA from germination on plants grown in vitro. All images reveal the fluorescent signal, and are SurfCut projections from 0 to 4 μm from the surface of the stem. Scale bars: 10 μm

A)

WT (Control)	-6 hrs	-5 hrs	-4 hrs	-3 hrs	-2 hrs	-1 hr	t0
-6 hrs	XXXXXX	0.1646	5.02e ⁻⁰⁶	< 2.2e ⁻¹⁶	< 2.2e ⁻¹⁶	7.10e ⁻⁰⁴	1.84e ⁻¹¹
-5 hrs	XXXXXX	XXXXXX	8.00e ⁻⁰⁷	< 2.2e ⁻¹⁶	< 2.2e ⁻¹⁶	0.00591	4.76e ⁻¹⁰
-4 hrs	XXXXXX	XXXXXX	XXXXXX	2.18e ⁻¹³	4.90e ⁻¹⁰	2.15e ⁻¹⁴	< 2.2e ⁻¹⁶
-3 hrs	XXXXXX	XXXXXX	XXXXXX	XXXXXX	0.3048	< 2.2e ⁻¹⁶	< 2.2e ⁻¹⁶
-2 hrs	XXXXXX	XXXXXX	XXXXXX	XXXXXX	XXXXXX	< 2.2e ⁻¹⁶	< 2.2e ⁻¹⁶
-1 hr	XXXXXX	XXXXXX	XXXXXX	XXXXXX	XXXXXX	XXXXXX	1.54e ⁻⁰⁵
0	XXXXXX	XXXXXX	XXXXXX	XXXXXX	XXXXXX	XXXXXX	XXXXXX

B)

WT (+ NPA)	-6 hrs	-5 hrs	-4 hrs	-3 hrs	-2 hrs	-1 hr	t0
-6 hrs	XXXXXX	0.1548	0.1552	7.18e ⁻⁰⁵	< 2.2e ⁻¹⁶	3.62e ⁻⁰⁴	< 2.2e ⁻¹⁶
-5 hrs	XXXXXX	XXXXXX	0.6853	8.33e ⁻⁰⁴	< 2.2e ⁻¹⁶	0.005563	< 2.2e ⁻¹⁶
-4 hrs	XXXXXX	XXXXXX	XXXXXX	9.04e ⁻⁰⁵	< 2.2e ⁻¹⁶	2.21e ⁻⁰⁴	< 2.2e ⁻¹⁶
-3 hrs	XXXXXX	XXXXXX	XXXXXX	XXXXXX	< 2.2e ⁻¹⁶	0.763	< 2.2e ⁻¹⁶
-2 hrs	XXXXXX	XXXXXX	XXXXXX	XXXXXX	XXXXXX	< 2.2e ⁻¹⁶	< 2.2e ⁻¹⁶
-1 hr	XXXXXX	XXXXXX	XXXXXX	XXXXXX	XXXXXX	XXXXXX	< 2.2e ⁻¹⁶
0	XXXXXX	XXXXXX	XXXXXX	XXXXXX	XXXXXX	XXXXXX	XXXXXX

Figure S4. *p*-value results for Kolmogorov-Smirnoff tests, comparing the distributions of CMT orientations under control conditions (A), or NPA conditions (B), between the different timepoints. The dataset used for this test was the results obtained with the Directionality plugin in Fiji. The null hypothesis for the Kolmogorov-Smirnoff test is “There are no differences between the two distributions”.

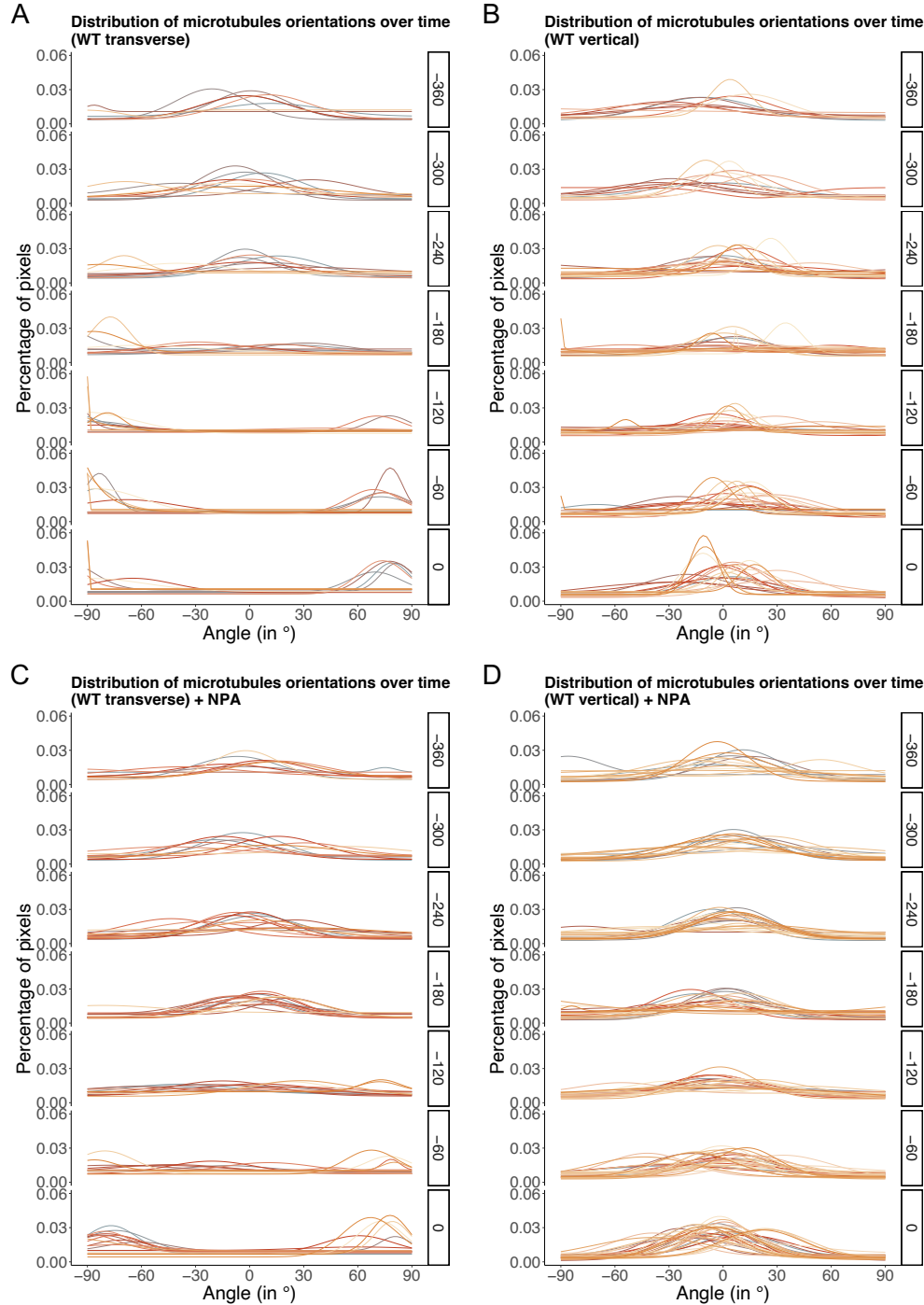


Figure S5. Evolution of CMT orientation over time in WT pre-mitotic cells from the stem, divided in four data subsets.

(A-D) The angle scale varies between -90° and $+90^\circ$, 0° being the transverse orientation to the stem axis. Each row represents the time before $t=0$ (last timepoint before the nuclear envelope breakdown). Each color-coded curve represents the results obtained for one cell. The dataset used is the same as the one used for Figures 1G and 2I. (A) Results obtained for cells that produce a preprophase band oriented along the stem axis (i.e. between -30° and 30°), grown on media without NPA. (B) Results obtained for cells that produce a preprophase band oriented transverse to the stem axis (i.e. between -60° and -90° , and between 60° and 90°), grown on media without NPA. (C) Similar to (A), for cells grown on NPA conditions. (D) Similar to (B), for cells grown on NPA conditions.

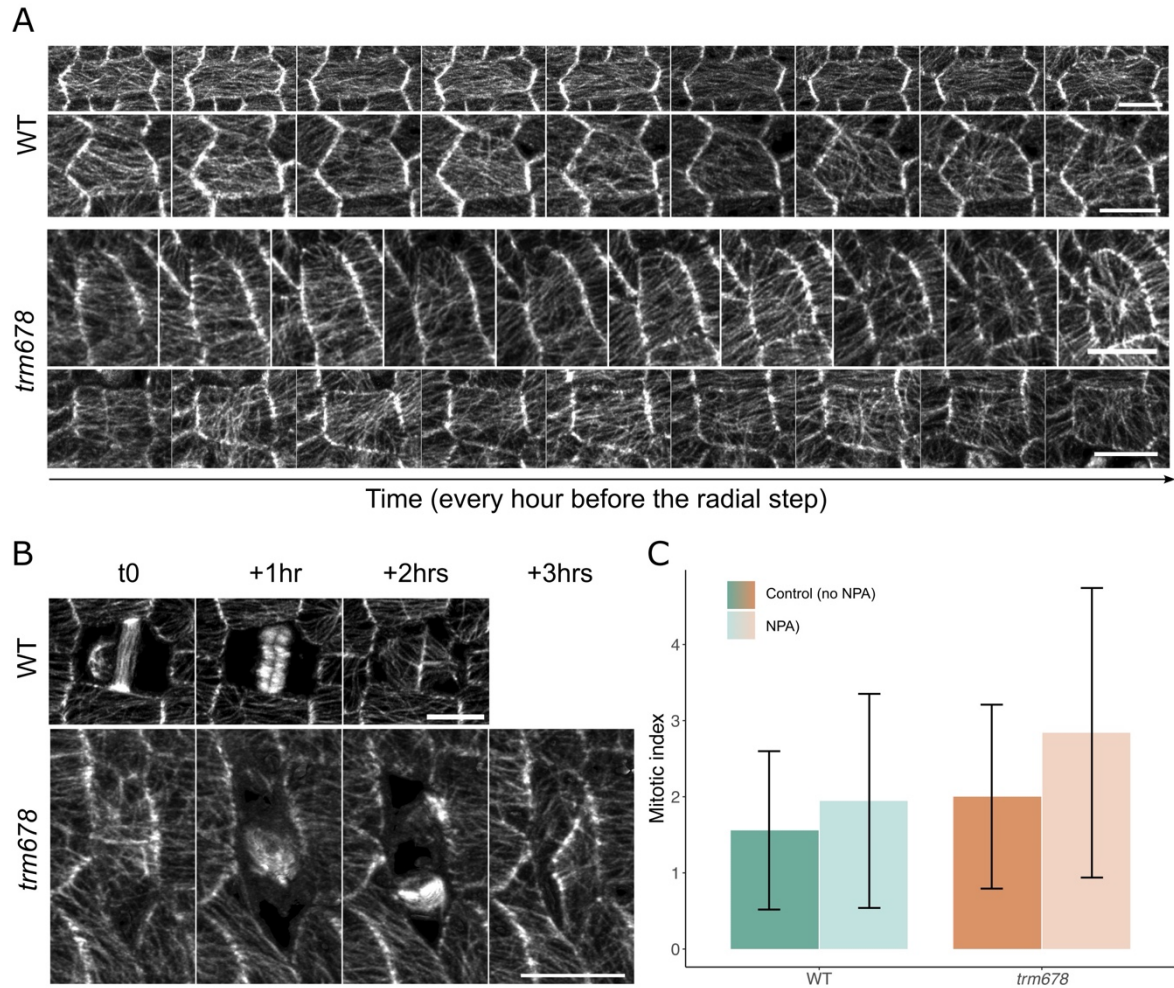


Figure S6. CMT dynamics and mitosis in WT and *trm678*

(A) CMT dynamics before the radial step in the WT and *trm678*. Images were taken every hour. (B) CMT behavior during division in a representative WT cell (top panel) and a representative *trm678* cell (bottom panel). The images are SurfCut projections between 0 and 4 μm from the surface of the stem, and the scale bars correspond to 10 μm . (C) Mitotic indexes for cells in both genetic background and in control, or NPA conditions. The mitotic index corresponds to the ratio between mitotic cells (where we can observe spindle or phragmoplast structures) and the total number of cells in the image. *trm678* cells have a slightly higher mitotic index than the WT, and the addition of NPA increases the mitotic index in both backgrounds. $n_{\text{WT, control}} = 12$; $n_{\text{WT, NPA}} = 5$; $n_{\text{trm678, control}} = 16$; $n_{\text{trm678, NPA}} = 9$.

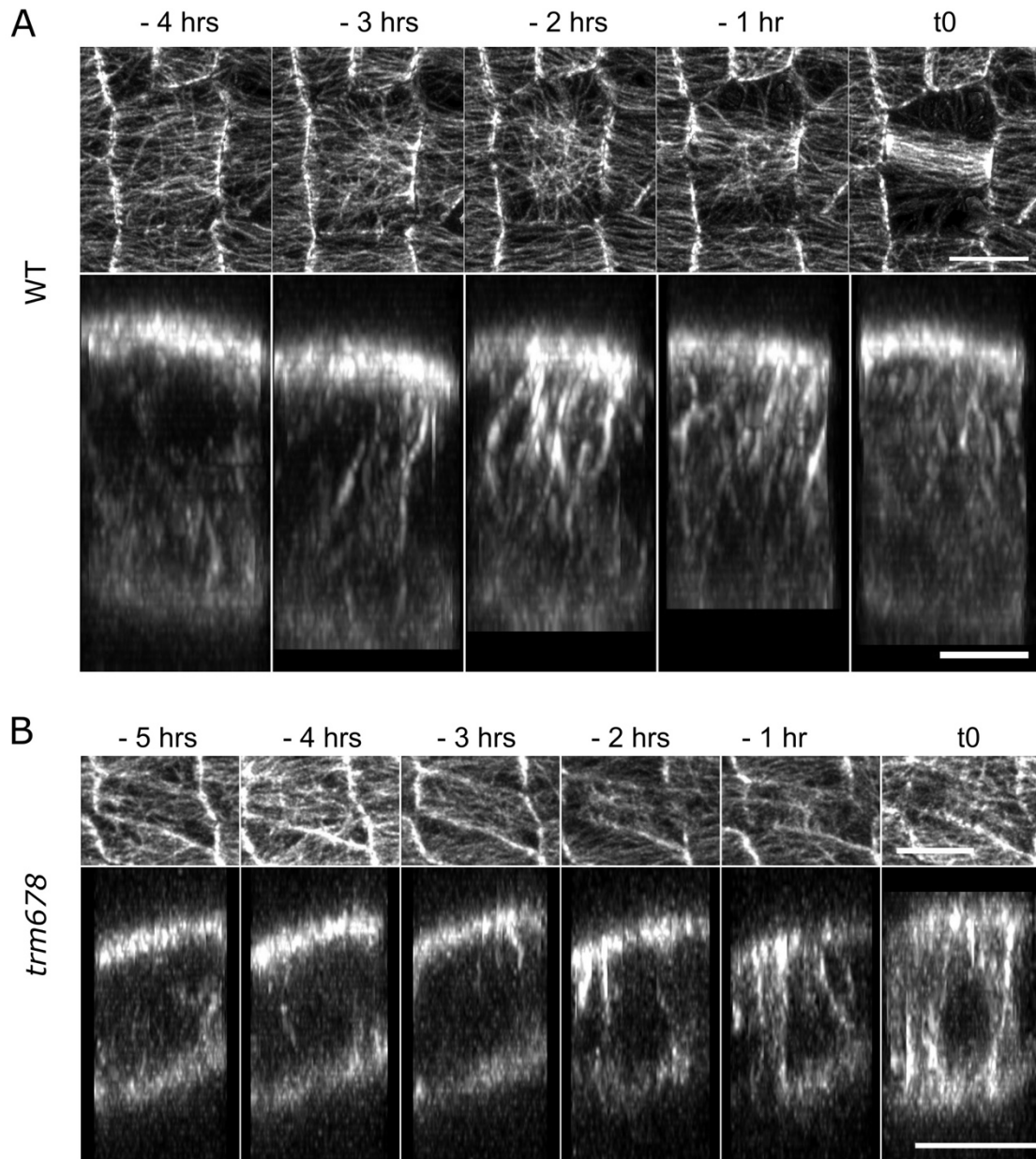


Figure S7. Other examples of the evolution of cytoplasmic microtubule content in pre-mitotic cells.

(A) Time-lapse images of pre-mitotic cells, the top panel being the cortical projection with SurfCut and the bottom panel an orthogonal projection through the cell. Cortex images are 8-bit, with the B&C range varying between 0 and 160, and orthogonal projections are 16-bit, with the B&C range varying between 0 and 2600. (B) Same as (A) but in *trm678* mutant cell. Note that this is an exceptional case where the radial step is short in *trm678*, which allows the visualization of the full sequence: interphase - radial step - mitosis, further showing the correlation between radial step and perinuclear microtubule accumulation. Scale bars: 10 μm (surface projections), 5 μm (XZ orthogonal projections).

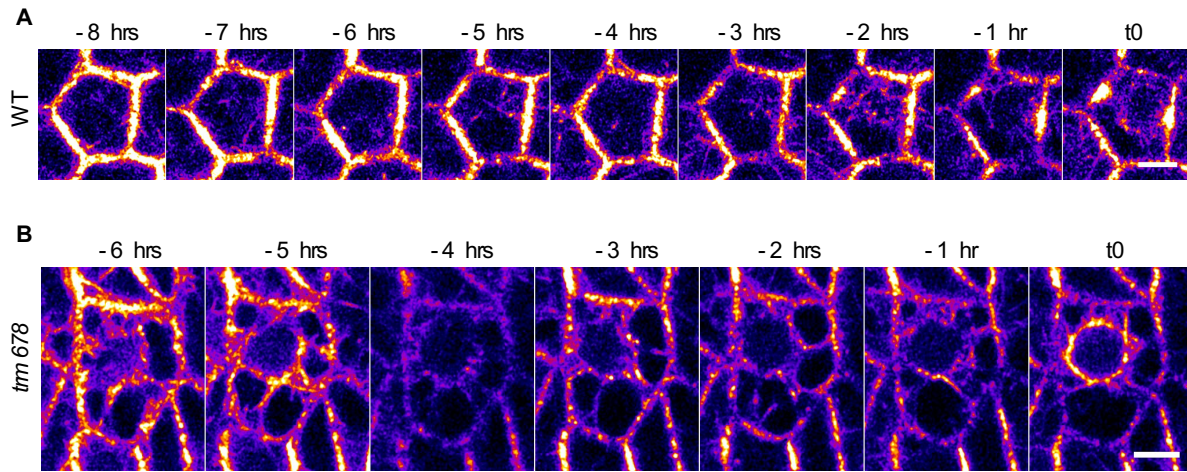


Figure S8. *pPDF1::mCitrine-MBD* signal at the equator of a cell from the stem overtime.
 (A,B) These images were made showing a single slice of the Z-stack in the middle of the cell.
 (A) WT cell: these 16-bit images are obtained using the fire Look-up table in Fiji, with the
 Brightness&Contrast values set between 0 and 1000. (B) *trm678* mutant cell: these 16-bit
 images are obtained using the fire Look-up table in Fiji, with the Brightness&Contrast values
 set between 0 and 3000. The scale bars correspond to 5 μm.

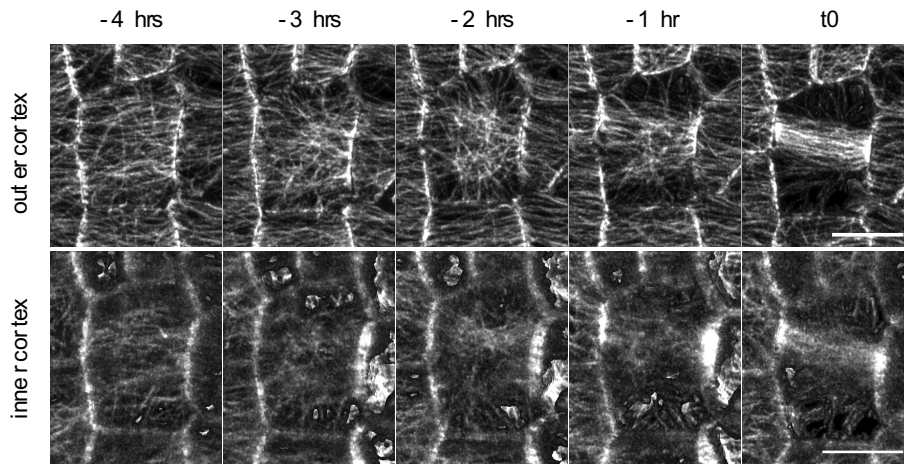
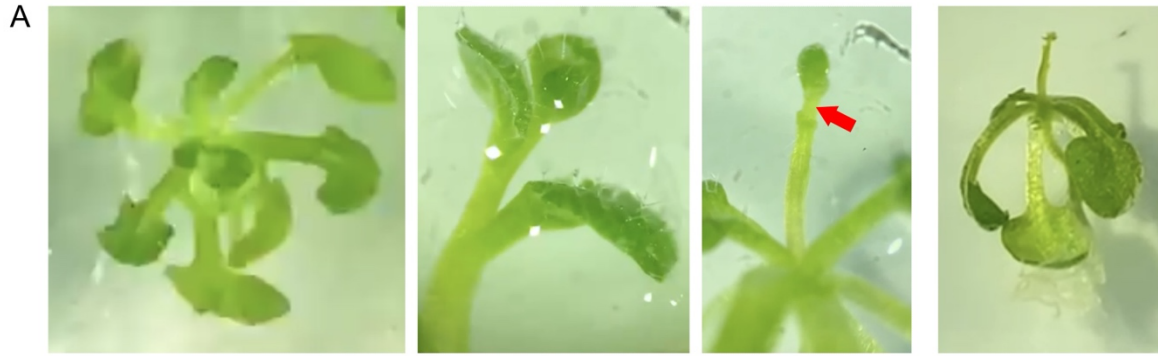


Figure S9. Cortical microtubule dynamics of a pre-mitotic cell, displaying the signal from the periclinal outer (top) and inner (bottom) cortex. The images are SurfCut projections of the *pPDF1::mCitrine-MBD* signal between 0 and 4 μm , either starting from the top (top images) or bottom (bottom images) of the cell. The signal from the inner cortex is noisier due to the weaker signal, and the more difficult extraction of the tissue surface. The scale bars are 10 μm .



B

	mCitrine	TdTomato
Laser (λ , power)	514 nm, 0.10 %	561 nm, 0.10 %
Main Beam Splitter	MBS 445/514/561/639	MBS 488/561
Secondary Beam Splitter	SBS SP 615	SBS SP 615
Emission Filters for the Airyscan detector	BP 420-480 + BP 495-550	Plate (transmission 100%)

Figure S10. Protocols: additional data

(A) Step-by-step representation of the stem sample preparation (left to right). First, select a seedling with a stem of around 1.5 cm in length and with a few unopened flower buds. The area of interest (the stem portion under the meristem) is often covered by a few organs. These organs are dissected out in order to expose the area of interest (red arrow). Finally, insert the roots and a few leaves inside the agar to fix the sample, while leaving the area of interest on top of the agar for it to be accessible to the microscope. (B) Airyscan detection parameters.